Skyrmions in Twisted Bilayer Graphene: Stability, Pairing, and Crystallization

Yves H. Kwan,[1] Glenn Wagner,[1,2] Nick Bultinck,[1,3] Steven H. Simon,[1] and S. A. Parameswaran[1]

[1]*Rudolf Peierls Centre for Theoretical Physics, Parks Road, Oxford, OX1 3PU, United Kingdom*
[2]*Department of Physics, University of Zurich, Winterthurerstrasse 190, 8057 Zurich, Switzerland*
[3]*Department of Physics and Astronomy, Ghent University, Krijgslaan 281, 9000 Ghent, Belgium*

(Received 20 January 2022; revised 13 June 2022; accepted 29 June 2022; published 29 July 2022)

We study the excitations that emerge upon doping the translationally invariant correlated insulating states in magic-angle twisted bilayer graphene at various integer filling factors ν. We identify parameter regimes where these are excitations associated with skyrmion textures in the spin or pseudospin degrees of freedom, and explore both short-distance pairing effects and the formation of long-range ordered skyrmion crystals. We perform a comprehensive analysis of the pseudospin skyrmions that emerge upon doping insulators at even ν, delineating the regime in parameter space where these are the lowest-energy charged excitations by means of self-consistent Hartree-Fock calculations on the interacting Bistritzer-MacDonald model. We explicitly demonstrate the purely electron-mediated pairing of skyrmions, a key ingredient behind a recent proposal of skyrmion superconductivity. Building upon this, we construct hopping models to extract the effective masses of paired skyrmions, and discuss our findings and their implications for skyrmion superconductivity in relation to experiments, focusing on the dome-shaped dependence of the transition temperature on the twist angle. We also investigate the properties of spin skyrmions about the quantized anomalous Hall insulator at $\nu = +3$. In both cases, we demonstrate the formation of robust spin or pseudospin skyrmion crystals upon doping to a finite density away from integer filling.

DOI: 10.1103/PhysRevX.12.031020

Subject Areas: Condensed Matter Physics
Strongly Correlated Materials
Superconductivity

I. INTRODUCTION

The experimental observation of an array of interaction-driven electronic phases in magic-angle twisted bilayer graphene (TBG) [1–4] has stimulated intense theoretical efforts to formulate a unifying physical description of their emergence from the interplay of topology, symmetry, and correlations. One promising route to a solution has close ties to the now-classic paradigm of strongly interacting electrons in Landau levels (LLs). As shown in Ref. [5], this so-called "strong-coupling" picture is rooted in the identification of an idealized limit with a $\mathrm{U}(4) \times \mathrm{U}(4)$ global symmetry that operates within the subspace of the eight central bands: The two U(4) symmetries rotate within quartets of topological Chern bands with Chern numbers $C = \pm 1$, respectively (see also Refs. [6–9]). Correlated insulating phases arise as a result of symmetry breaking within this (almost) degenerate subspace, in a manner analogous to the formation of quantum Hall ferromagnetism in integrally filled LLs [10]. This perspective receives support from the detection of a quantized anomalous Hall insulator (QAHI) at $\nu = +3$ [11–13] and various magnetic-field stabilized Chern insulators at other fillings [4,14–19]. While a purely strong-coupling treatment does not completely resolve the experimental puzzles surrounding TBG, it serves as a natural starting point for considering how various physically realistic corrections influence the competition between ordered states. In this manner, it can aid in the identification of new and distinct broken-symmetry phases that are not accessible in any obvious way from the weakly interacting limit, but can be viewed as descending from strong-coupling ferromagnetic orders in a natural, albeit nontrivial, fashion as the system is tuned toward the physically relevant intermediate-coupling regime [20,21].

The underlying topology of TBG not only influences the selection of correlated states, but also leaves its fingerprint on the nature of their excitations—suggesting a tantalizing link between insulating behavior at integer filling and superconducting behavior away from it [22–26]. In this vein, neutral excitations of the QAHI have been predicted to inherit striking characteristics from the symmetry-breaking and topological properties of the parent insulator [27–30]. Given the intimate connection to quantum Hall ferromagnetism (QHFM), the strong-coupling insulators of TBG can also be expected to host charged excitations in the

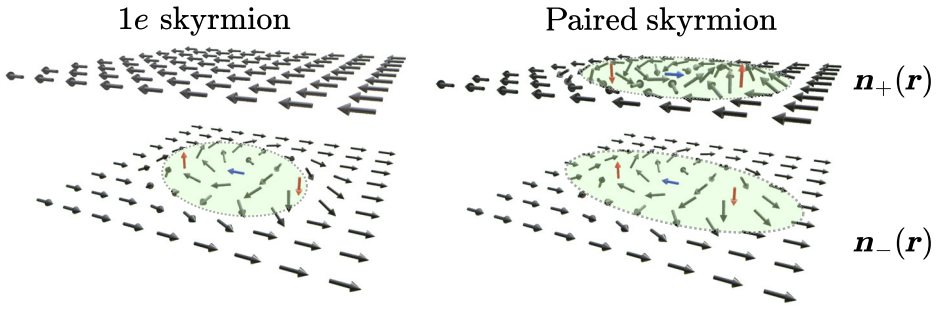

FIG. 1. Caricature of $1e$ skyrmions and paired $2e$ skyrmions at $\nu = 0$. Arrows depict the local orientation of pseudospins $\boldsymbol{n}_\pm(\boldsymbol{r})$ in the two Chern sectors ($C = \pm 1$) as defined in Eq. (2) for skyrmions about the KIVC insulator at charge neutrality. Green shaded regions show where the doped electric charge is localized. Blue arrows indicate the center of the skyrmions, and red arrows denote where pseudospins are aligned along the z axis.

form of spin or pseudospin textures known as skyrmions or merons [22,31–38]. For example, under certain conditions, additional charge carriers can enter the QAHI as skyrmions rather than as single spin-flip quasiparticles. The situation is richer at even integer fillings since the intricate structure afforded by the approximate $\mathrm{U}(4) \times \mathrm{U}(4)$ symmetry and the associated anisotropies is more apparent here. Besides spin, the relevant textures now also have access to the valley and sublattice degrees of freedom (additional "flavors"), leading to the emergence of pseudospin skyrmions. The importance of a detailed understanding of such topological objects is underscored by a recent proposal [22] of purely electronic superconductivity arising from bosonic "paired skyrmions" [39,40] of charge $2e$ (see Fig. 1), whose stabilization arises from the particular features of the strong-coupling Hamiltonian. Such unconventional Cooper pairs may be relevant for understanding the various superconducting domes in TBG [2–4,41–45], whose properties and origins remain the subject of intense debate.

To date, however, the investigation of such flavor textures has been limited to either analyses of the effective nonlinear sigma model (NLSM) [22] or numerical studies of a simplified model mimicking the gross features of the central bands [23]. While such studies provide qualitative insight, a systematic exploration of these charged textures within a realistic microscopic model of TBG remains an outstanding challenge. There is no guarantee that topological textures are relevant once unavoidable complications such as momentum space structure, finite kinetic energy, and the presence of a moiré lattice are accounted for. (A recent study of domain-wall textures in the $\nu = +3$ QAHI, where microscopic energetics significantly alter properties of the topologically mandated electronic boundary modes, suggests that it is indeed important to consider such details [46].) This microscopic demonstration is the lacuna which we address in this paper, by directly probing the nature of (pseudo) spin skyrmions using unbiased self-consistent Hartree-Fock (HF) calculations within the interacting Bistritzer-MacDonald (BM) model [47,48]. This requires us to consider completely unrestricted Slater determinants, allowing for full breaking of moiré translation symmetry. This is a challenging task even within the constrained variational space of the HF mean-field ansatz, but one that we pursue successfully below.

We have three main objectives in this work: first, to provide a proof-of-principle demonstration of skyrmion pairing in an appropriately chosen limit of a microscopic model of TBG; second, to investigate whether such a pairing can result in superconducting phenomenology consistent with that seen in experiment (most notably, the dome-shaped dependence of the superconducting transition temperature T_c on the twist angle [41]); third, to establish the regime in parameter space over which pairing survives away from the idealized limit. We also consider a subsidiary set of issues pertaining to the emergence of skyrmions at other fillings, and their formation of long-range ordered structures [49–51] when doped into TBG at a finite density.

Within a HF treatment of the interacting BM model, we find that pseudospin skyrmion pairing does indeed occur about even integer filling and at sufficiently small chiral ratio, and in qualitative agreement with the predictions of the NLSM. Paired skyrmions are lower in energy than particle excitations for small chiral ratio, with relatively better energetics at charge neutrality than at $|\nu| = 2$. For chiral ratios approaching the realistic values, they become energetically unfavorable and harder to stabilize within mean-field theory. External perturbations such as strain and substrate, as well as increased screening of interactions, tend to also have the same effect. We devise an effective skyrmion hopping model to estimate the effective masses, and find that the corresponding superconducting critical temperature T_c [52] can be larger than typical scales observed experimentally. However, more detailed comparison of the twist-angle dependence is complicated by the sensitivity of the results to how electron interactions are incorporated (i.e., the "subtraction scheme," to be explained in Sec. II A). We critically discuss our findings in the context of experiments, and conclude that, at least for some of the samples, skyrmion pairing is unlikely to be

mechanism for superconductivity. For the QAHI at $|\nu| = 3$, we demonstrate the formation of spin skyrmions for doping of single charges, and various spin texture lattices at larger dopings.

The balance of this paper is organized as follows. After reviewing the basics of the NLSM and strong-coupling picture of TBG in Sec. II, we focus on the pseudospin skyrmions about the spinless insulator at charge neutrality ($\nu = 0$) in Sec. III. Via an effective skyrmion hopping model, we further estimate the dispersion and effective mass of delocalized skyrmions. We also briefly address the situation at $|\nu| = 2$ in the spinful case. In Sec. IV, we discuss the properties of spin skyrmions and spin texture lattices at $|\nu| = 3$ about the QAHI. We end with a discussion in Sec. V.

II. THEORETICAL CONSIDERATIONS

In this section, we review the key concepts that underpin the existence and properties of skyrmions about the strong-coupling insulators in TBG [5,8,53].

A. Interacting BM model

The starting point is the continuum BM model $\hat{H}^{\mathrm{BM}}$ which generates the single-particle moiré bands of TBG in the moiré Brillouin zone (MBZ) [47]. Details of the model are relegated to Appendix A in the Supplemental Material [54], but we mention here the important parameters which will influence the skyrmions. The interlayer coupling is parametrized through two sublattice-dependent hopping constants w_{AA} and w_{AB} reflecting corrugation effects in the superlattice. We fix $w_{AB} = 110$ meV but consider variable w_{AA}, thereby tuning the value of the chiral ratio $\kappa \equiv w_{AA}/w_{AB}$. The estimated values for κ in the literature range from 0.5 to 0.8 [55–57]. The kinetic bandwidth is minimal when the twist angle θ is close to the magic angle, which is weakly dependent on κ. While the physical relevance of θ as a tuning parameter is obvious, it will prove theoretically useful to vary w_{AA} to control deviations from the fully symmetric theory, to be described below. (Note that it has been argued that the effective value of w_{AA} may be susceptible to renormalization toward the chiral limit [58] $\kappa = 0$ due to the effects of remote bands; thus, tuning w_{AA} may be viewed as phenomenologically modeling this downward renormalization [9].)

Sometimes, we also incorporate heterostrain [20,59,60] with strength ϵ and a sublattice potential of strength Δ [61]. In the absence of such single-particle perturbations, the point group is D_6, which includes $\hat{C}_{2z}$, $\hat{C}_{3z}$, and $\hat{M}$ (in-plane rotation about the x axis). Accounting for both valley and spin degrees of freedom, the BM model contains a $\mathrm{U}(2)_K \times \mathrm{U}(2)_{K'}$ flavor symmetry which includes charge or valley conservation and independent SU(2) spin rotations within each valley. Naturally, a spinless time-reversal symmetry (TRS) $\hat{\mathcal{T}} = \tau_x \hat{\mathcal{K}}$ is also present, where $\hat{\mathcal{K}}$ is the complex conjugation operator. Upon neglecting the weak relative rotation of the Dirac cones in the two layers, there is also a particle-hole symmetry (PHS) $\hat{\mathcal{P}}$ [62–64]. Throughout this work, we focus solely on the central eight bands and project out the remote bands which are separated by a large band gap. (Although, see the preceding comments on their possible role in adjusting w_{AA}.)

Repulsive interactions are implemented by augmenting the BM model with dual-gate screened density-density Coulomb interactions $V(q) = (e^2/2\epsilon_0\epsilon_r q)\tanh q d_{\mathrm{sc}}$, where the relative permittivity $\epsilon_r = 10$ and the screening length $d_{\mathrm{sc}} = 25$ nm [5]. By neglecting subleading "intervalley Hund's couplings," which scatter electrons between valleys, we retain the global $\mathrm{U}(2)_K \times \mathrm{U}(2)_{K'}$ symmetry.

Note that interactions may alter the one-body terms somewhat, leading to a total effective single-particle dispersion $\hat{H}^{\mathrm{SP}}$ [5,7,8,64–66]. The precise correction depends on the choice of "subtraction scheme," which arises as follows (a more detailed exposition can be found in Appendix A of Ref. [54]). Including only normal-ordered interactions within the central-band subspace neglects contributions from the remote bands. Furthermore, some interactions are double counted because the hopping parameters of graphene (e.g., from density-functional-theory calculations) are obtained self-consistently with filled valence bands. A convenient parametrization to remedy this and restore PHS is in terms of a reference density matrix P^0. There is no unique prescription for fixing P^0, and we consider three choices that have been used in the literature: (i) the "average," (ii) "charge neutrality" (CN), and (iii) "graphene" schemes. This nomenclature is motivated by how P^0 is constructed: (i) $P^0 \propto I$, (ii) P^0 consists of the filled valence BM bands, and (iii) P^0 consists of the filled valence bands of decoupled layers of graphene. Most of the initial discussion on skyrmions is based on the average scheme, which leads to no corrections when interactions are recast in the strong-coupling form that highlights the strong-coupling hierarchy of scales (see Sec. II B and Appendix A of Ref. [54]). The other two schemes are analyzed in more detail in Sec. III D.

B. Strong-coupling hierarchy

Since the typical Coulomb scale exceeds the kinetic bandwidth, the BM band basis may not be the most natural one in which to understand interaction physics. A more appropriate choice that reveals the underlying topological character of the bands is furnished by the Chern basis obtained by diagonalizing the sublattice operator σ_z [5]. Each band is predominantly polarized on one sublattice, which allows us to label the central bands with sublattice σ, valley τ, and spin s. Combining these into a single index α, we can write the Bloch functions as $|\psi_\alpha(\boldsymbol{k})\rangle = e^{i\boldsymbol{k}\cdot\hat{\boldsymbol{r}}}|u_\alpha(\boldsymbol{k})\rangle$ with associated creation operators $\hat{d}^\dagger_\alpha(\boldsymbol{k})$. Crucially, these bands have Chern number $C = \sigma_z\tau_z$ [Fig. 2(a)].

The link to QHFM is sharpened in the well-studied chiral limit $\kappa = 0$ [58,67], where the kinetic bandwidth becomes

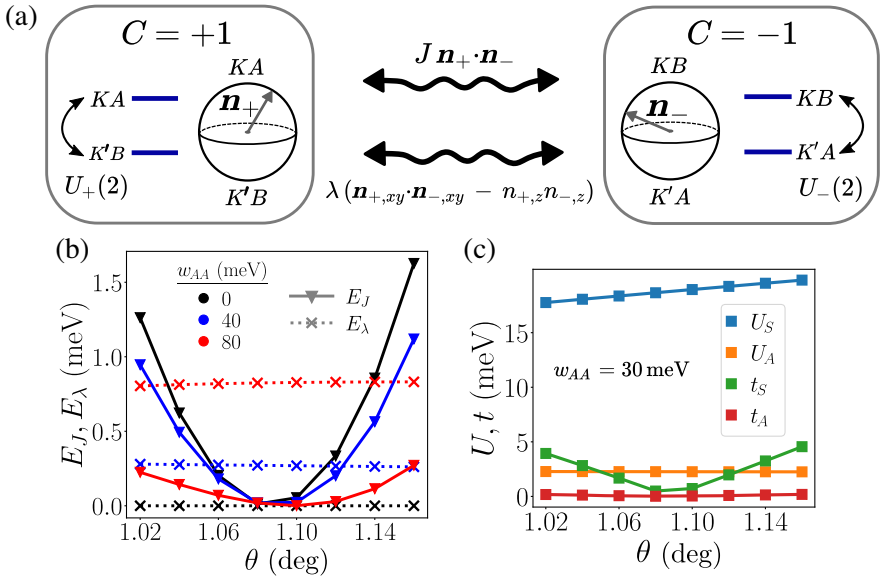

FIG. 2. Strong-coupling hierarchy and Chern pseudospins. (a) Schematic of Chern sectors with $C = \pm 1$. In the isotropic limit, there is a $\mathrm{U}(2) \times \mathrm{U}(2)$ symmetry [$\mathrm{U}(4) \times \mathrm{U}(4)$ with spin]. At charge neutrality for a generalized ferromagnet with net $C = 0$, one can define pseudospins $\boldsymbol{n}_\pm$. The dominant corrections can be captured as anisotropies J, λ (wiggly lines) which couple the Chern sectors and partially lift the symmetry. (b) NLSM parameters $E_J = JA_{\mathrm{UC}}$ (triangles), $E_\lambda = \lambda A_{\mathrm{UC}}$ (crosses) as a function of twist angle θ, and interlayer hopping parameter w_{AA}, where A_{UC} is the moiré unit cell area. The pseudospin stiffness $\rho_{\mathrm{PS}} \simeq 1.5$ meV calculated in the isotropic limit does not depend on w_{AA} and subtraction scheme (see Appendix A in Ref. [54]), and is largely insensitive to θ. (c) Strong-coupling energy scales U_S, U_A, t_S, t_A as a function of θ and w_{AA}. All quantities are calculated using the average subtraction scheme.

exactly zero at the magic angle and the Chern bands become completely sublattice polarized. In addition, the new chiral symmetry $\{\sigma_z, H^{\mathrm{BM}}\}$, in concert with $\hat{C}_{2z}\hat{\mathcal{T}}$ and $\hat{\mathcal{P}}$, heavily constrains the form factors $\Lambda_{\alpha,\beta}(\boldsymbol{k},\boldsymbol{q}) \equiv \langle u_\alpha(\boldsymbol{k})|u_\beta(\boldsymbol{k}+\boldsymbol{q})\rangle$ to be diagonal and to depend only on the Chern number: This allows us to write $\Lambda_{\alpha,\beta}(\boldsymbol{k},\boldsymbol{q}) = \Lambda^S(\boldsymbol{k},\boldsymbol{q})\delta_{\alpha\beta}$ with [5]

$$\Lambda^S(\boldsymbol{k},\boldsymbol{q}) = F^S(\boldsymbol{k},\boldsymbol{q})e^{i\phi^S(\boldsymbol{k},\boldsymbol{q})\sigma_z\tau_z}, \tag{1}$$

where the superscript S denotes "symmetric." In the chiral-flat limit where the effective dispersion $\hat{H}^{\mathrm{SP}}$ is neglected, Eq. (1) implies a huge $\mathrm{U}(4)_{C=1} \times \mathrm{U}(4)_{C=-1}$ symmetry, as can be seen by checking the invariance of the density operator $\hat{\rho}^S(\boldsymbol{q}) = \sum_{\boldsymbol{k}} \hat{\boldsymbol{d}}^\dagger(\boldsymbol{k})\Lambda^S(\boldsymbol{k},\boldsymbol{q})\hat{\boldsymbol{d}}(\boldsymbol{k}+\boldsymbol{q})$ under independent Chern-number-preserving rotations. Remarkably, at $\nu = 0$ one can prove the existence of exact Slater determinant ground states, which simply involve uniformly polarizing any four orthogonal directions within the Chern quartets ("ferromagnets") [5,8]. Hence, the chiral-flat limit is also referred to as the isotropic limit.

The utility of the chiral-flat limit lies in the existence of a hierarchy of scales which permits corrections to be treated perturbatively within the manifold of strong-coupling ferromagnets [5,8]. The energy scale of the full symmetry group is U_S, and the main competing scales are the single-particle inter-Chern tunneling (t_S) and deviation from chirality (U_A), with intra-Chern dispersion (t_A) being subleading [see Fig. 2(d) and Appendix A in Ref. [54]]. Focusing for simplicity on the spinless insulator at neutrality such that the parent symmetry group is $\mathrm{U}(2) \times \mathrm{U}(2)$, the effects of the above perturbations can be captured via anisotropies with positive strengths J and λ, respectively (i.e., energy scales $E_J = A_{\mathrm{UC}}J$ and $E_\lambda = A_{\mathrm{UC}}\lambda$, where A_{UC} is the moiré unit cell area). It turns out that the states that get energetically selected by these terms have total $C = 0$. Defining an intra-Chern Pauli triplet $\boldsymbol{\eta} = (\sigma_x\tau_x, \sigma_x\tau_y, \tau_z)$, we can parametrize the strong-coupling ferromagnets residing in the Chern-neutral sector with two Chern-filtered pseudospins

$$\boldsymbol{n}_\pm(\boldsymbol{k}) \equiv \langle\Psi|\hat{\boldsymbol{d}}^\dagger(\boldsymbol{k})\boldsymbol{\eta}\frac{1 \pm \sigma_z\tau_z}{2}\hat{\boldsymbol{d}}(\boldsymbol{k})|\Psi\rangle, \tag{2}$$

which are independent of $\boldsymbol{k}$ [Fig. 2(a)]. Inter-Chern tunneling generates superexchange inducing an antiferromagnetic (AFM) coupling between the two pseudospins, while a finite κ manifests as an AFM coupling in plane, and a FM coupling out of plane. Both break the chiral-flat symmetry to distinct U(2) subgroups. The resulting ground state with $\boldsymbol{n}_+ = -\boldsymbol{n}_-$ [and hence, valley-$\mathrm{U}(1)_V$ degeneracy] is the Kramers intervalley-coherent insulator (KIVC), so called because it preserves a modified TRS $\hat{\mathcal{T}}' = \tau_y\hat{\mathcal{K}}$. An equivalent description of the spinless KIVC is via its density matrix $P = \frac{1}{2}(1 + Q)$, where

$$Q_{\mathrm{KIVC}} = \sigma_y(\tau_x \cos\phi_{\mathrm{IVC}} + \tau_y \sin\phi_{\mathrm{IVC}}) \tag{3}$$

is parametrized through the IVC angle ϕ_{IVC}.

C. Nonlinear sigma model and pseudospin textures

To understand low-energy excitations and spatially nonuniform configurations, it is useful to consider a continuum NLSM description purely in terms of the pseudospins [22]. The energy functional, familiar from QHFM, is

$$E[\boldsymbol{n}_+, \boldsymbol{n}_-] = \int d^2\boldsymbol{r}\left[\frac{\rho_{\mathrm{PS}}}{2}((\nabla\boldsymbol{n}_+)^2 + (\nabla\boldsymbol{n}_-)^2) + (J+\lambda)\boldsymbol{n}_+\cdot\boldsymbol{n}_- - 2\lambda n_+^z n_-^z\right] + \frac{1}{2}\int d^2\boldsymbol{r}'\delta\rho(\boldsymbol{r})V(\boldsymbol{r}-\boldsymbol{r}')\delta\rho(\boldsymbol{r}'), \tag{4}$$

where ρ_{PS} is the pseudospin stiffness in the isotropic limit, and $\delta\rho = \delta\rho_+ + \delta\rho_-$ consists of the topological charge (Pontryagin index) densities of the two Chern sectors

$$\delta\rho_\pm(\boldsymbol{r}) = \pm e\rho_{\mathrm{top},\pm}(\boldsymbol{r}) = \pm\frac{e}{4\pi}\boldsymbol{n}_\pm\cdot\partial_x\boldsymbol{n}_\pm\times\partial_y\boldsymbol{n}_\pm. \tag{5}$$

The skyrmion number is given by

$$N_{\mathrm{top},\pm} = \int d^2\boldsymbol{r}\rho_{\mathrm{top},\pm}(\boldsymbol{r}), \tag{6}$$

where skyrmions and antiskyrmions have $N_{\mathrm{top}} = +1$ and $N_{\mathrm{top}} = -1$, respectively.

The NLSM parameters J, λ, ρ_{PS} are plotted in Fig. 2, with explicit expressions supplied in Appendix A of Ref. [54]. In the "average scheme" described there, the superexchange J has a prominent minimum and nearly vanishes around $\theta \simeq 1.08°$, coincident with where the bare BM bandwidth is smallest. λ is a monotonically increasing function of w_{AA} and is largely insensitive to θ. The pseudospin stiffness $\simeq$1.3 meV is a property of the maximally symmetric manifold and has a very weak dependence on twist angle. While there are sizable regions where $\lambda > J$, this ordering of scales occurs only for the average scheme where J is directly tied to the bare BM scale, which is substantially smaller than the bandwidth obtained via STM measurements of the van Hove singularities in the density of states [68–72]. Therefore, we are mostly interested in the case $J \gtrsim \lambda$, which is conducive to skyrmion pairing as we explain below.

Consider first the isotropic limit $J = \lambda = 0$ where the Chern sectors decouple. The ground state at $\nu = 0$ is specified by free choices of uniform pseudospins $\boldsymbol{n}_\pm^0$. An additional charge enters as a $1e$ skyrmion (in one of the Chern sectors) rather than a particlelike excitation if the energy for a well-separated skyrmion-antiskyrmion pair ($8\pi\rho_{\mathrm{PS}}$) exceeds the particle-hole gap (Δ_{PH}). We can use the infinite-size Polyakov solution [31] which minimizes the gradient energy because of the lack of any Zeeman-like term, meaning that the texture prefers to expand to minimize the Coulomb term.

Reintroducing dispersion leads to an effective AFM coupling J, constraining the parent ground state $\boldsymbol{n}_+^0 = -\boldsymbol{n}_-^0$ which now belongs to an SO(3) manifold. A skyrmion of radius R_s in, say, $\boldsymbol{n}_+$ now experiences a Zeeman penalty $\propto R_s^2$ arising from misalignment with $\boldsymbol{n}_-^0$. The skyrmion becomes finite with a size determined from the competition between J and the interaction term. (Note that in order to avoid divergences with system size, the tails of the skyrmion profile must decay faster in space than the Polyakov ansatz [22,32,73].) For large enough J, the skyrmion shrinks and crosses over to an ordinary particlelike excitation. Having instead a finite λ leads to similar conclusions, except with a different residual SU(2) manifold. Including both perturbations restricts the insulator to a KIVC parametrized by a U(1) valley angle.

Adding instead a net charge of $|Q| = 2e$ to the system leads to substantially different conclusions. In the scenario with nonzero J, the AFM interaction leads to the pairing of a skyrmion in $\boldsymbol{n}_+$ with an antiskyrmion in $\boldsymbol{n}_-$ (the total charge is $2e$, a crucial consequence of the opposite assignment of Chern numbers). To see this, note that the AFM inter-Chern coupling is completely satisfied if the two textures are centered at the same position with exactly the same profile such that $\boldsymbol{n}_{\mathrm{pair}}(\boldsymbol{r}) \equiv \boldsymbol{n}_+(\boldsymbol{r}) = -\boldsymbol{n}_-(\boldsymbol{r})$. In this case, the resulting "paired $2e$ skyrmion" dilates without limit to avoid the Coulomb self-energy. Hence, an $\boldsymbol{n}_+$ skyrmion and an $\boldsymbol{n}_-$ antiskyrmion will bind for any positive value of J, even though the underlying electron interaction is purely repulsive. A paired-skyrmion configuration preserves $\hat{\mathcal{T}}'$ symmetry, which is a useful numerical diagnostic.

In the presence of an additional λ term, the paired skyrmion experiences an energy penalty $\propto R_s^2$ from regions where $\boldsymbol{n}_{\mathrm{pair}}(\boldsymbol{r})$ is not lying in plane. This not only leads to a finite size, but also elongates the texture somewhat to reduce the area spent pointing out of plane. When λ is comparable to J, the texture deforms to resemble the topologically equivalent configuration of two paired $1e$ merons separated by a finite distance. This can be understood as the λ term shrinking the costly $\boldsymbol{n}_{\mathrm{pair}}\|\hat{z}$ regions such that they become the cores of the merons (see red arrows in Fig. 1). If λ/J is sufficiently large, pairing is no longer favorable.

D. Skyrmion superconductivity

We now assume that the microscopic parameters are chosen such that charges enter as skyrmions rather than particles. $1e$ skyrmions from opposite Chern sectors attract to form paired skyrmions. Even if particle excitations are slightly lower in energy, this typically occurs in a small region of the MBZ centered at Γ_M. Hence, above a critical

doping, additional charges are expected to form skyrmions [22].

A nonzero superconducting T_c requires a finite boson effective mass M_{pair}, which can be motivated within the phenomenological picture of a pair of coupled quantum Hall ferromagnets [22] in equal and opposite magnetic fields. A single $1e$ skyrmion feels a net magnetic field and hence has a flat-band dispersion. On the other hand, the magnetic fields experienced by a paired skyrmion cancel out. To understand the generation of an effective mass in this case, imagine a paired skyrmion propagating at some velocity v. The Lorentz forces in the two sectors act to push the constituent $1e$ skyrmions in opposite directions, which is counteracted by a restoring force depending linearly on J and the separation (λ is assumed small). By balancing the two, one can deduce that M_{pair} is inversely proportional to J. Therefore, the paired skyrmions condense with a finite superfluid stiffness and associated Berezenskii-Kosterlitz-Thouless transition temperature [52]

$$T_c = \frac{\nu\pi\hbar^2}{2k_B A_{\text{UC}} M_{\text{pair}}} = \frac{\nu J A_{\text{UC}}}{2k_B}. \tag{7}$$

We define a corresponding filling-independent energy scale $E_c = k_B T_c/\nu$, which equals $E_J/2$ in this framework. Above, ν should be taken to be the doping relative to the integer filling of interest.

Note the sensitive dependence on the superexchange J, which potentially provides a litmus test for the applicability of this mechanism to realistic samples of TBG. Namely, experiments observe a superconducting dome in T_c as a function of the twist angle, which peaks around $\theta = 1.08°$ [41]. The value of J, and indeed the effective mass as computed independently in Sec. III D, are also affected by θ through the evolution of the bandwidth and character of the BM bands. However, as we discuss later, the precise relationship is subtle and differs based on the choice of interaction. In particular, while the nature of the ordered normal state at $\nu = 0$ is unambiguous, depending only on the signs of J and λ, finer details such as skyrmion effective masses are susceptible to the specifics of the subtraction scheme (see Appendix A in Ref. [54]).

E. Numerical methods

Underpinning the discussion in the following sections are explicit mean-field solutions $|\phi\rangle$ for the (pseudo) spin skyrmions constructed using unbiased self-consistent HF calculations. Since such configurations break translation symmetry and flavor rotation symmetries, the HF density matrix takes the most general form

$$P_{\boldsymbol{k}\tau s\sigma;\boldsymbol{k}'\tau' s'\sigma'} = \langle \hat{d}^\dagger_{\boldsymbol{k}\tau s\sigma} \hat{d}_{\boldsymbol{k}'\tau' s'\sigma'} \rangle. \tag{8}$$

The MBZ momenta $\boldsymbol{k}$ take discrete values due to the finite system dimensions L_1, L_2 measured in units of the moiré lattice vectors $\boldsymbol{a}_1^M, \boldsymbol{a}_2^M$. Throughout this work, we take $L = L_1 = L_2$ so that a nondegenerate moiré band can accommodate L^2 electrons. The filling is fixed by the constraint $\mathrm{Tr}P = (4+\nu)L^2 = (4+\nu_0)L^2 + N$, where ν_0 is the parent integer filling factor, and N represents the number of additional doped electrons. We typically initialize the calculations with random initial projectors and accelerate convergence using the optimal damping algorithm [74]. Near $\nu = 0$, we neglect spin for simplicity and hence omit the index s when calculating both skyrmion and particle excitations.

For spin textures about the QAH state, the local order parameter is simply the local spin density

$$\boldsymbol{S}(\boldsymbol{r}) = \sum_{ss'\tau I} \langle \hat{\psi}^\dagger_{\tau s I}(\boldsymbol{r}) \boldsymbol{s}_{ss'} \hat{\psi}_{\tau s' I}(\boldsymbol{r}) \rangle, \tag{9}$$

where $\boldsymbol{s}$ is a Pauli triplet in spin space, and $I = \{1A, 1B, 2A, 2B\}$ labels the types of electrons living on different layers or sublattices. Replacing $\boldsymbol{s}$ by the identity gives the local charge density. The real-space fermion creation operator is defined in terms of the Chern basis as

$$\hat{\psi}^\dagger_{\tau s I}(\boldsymbol{r}) = \sum_{\boldsymbol{k}\sigma} \langle \psi_{\tau s\sigma}(\boldsymbol{k}) | \boldsymbol{r}; I \rangle \hat{d}^\dagger_{\tau s\sigma}(\boldsymbol{k}). \tag{10}$$

For pseudospin textures, the natural extension is the "diagonal" Chern-filtered pseudospin density

$$\boldsymbol{n}_C^{\text{diag}}(\boldsymbol{r}) = \sum_I \langle \hat{\boldsymbol{\psi}}^\dagger_I(\boldsymbol{r}) \frac{1 + C\tau_z\sigma_z}{2} \boldsymbol{\eta} \hat{\boldsymbol{\psi}}_I(\boldsymbol{r}) \rangle, \tag{11}$$

where spin is dropped, and $\boldsymbol{\eta}$ is the triplet of pseudospinor Paulis defined above Eq. (2). The net global Chern polarization is defined by the difference in fractional occupation in each Chern sector. Above, the Chern band-filtered real-space creation operator is

$$[\hat{\psi}^\dagger_I(\boldsymbol{r})]_{\tau\sigma} = \sum_{\boldsymbol{k}} \langle \psi_{\tau\sigma}(\boldsymbol{k}) | \boldsymbol{r}; I \rangle \hat{d}^\dagger_{\tau\sigma}(\boldsymbol{k}), \tag{12}$$

where $\tau\sigma$ labels the Chern band. However, the in-plane components of Eq. (11) identically vanish in the chiral limit $\kappa = 0$, where the Chern basis becomes completely sublattice polarized. For example, for the $C = +1$ Chern sector, $n_{+,x}$ and $n_{+,y}$ should measure coherence between the KA and $K'B$ bands, but $[\hat{\psi}^\dagger_I]_{KA}$ ($[\hat{\psi}^\dagger_I]_{K'B}$) is nonzero only when $I = 1A, 2A$ ($1B, 2B$).

To remedy this, we occasionally consider an alternative definition that includes off-diagonal terms in the layer or sublattice degrees of freedom

$$\boldsymbol{n}_C^{\mathrm{off}}(\boldsymbol{r}) = \sum_{II'} \langle \hat{\boldsymbol{\psi}}_I^\dagger(\boldsymbol{r}) \frac{1 + C\tau_z\sigma_z}{2} \boldsymbol{\eta} \hat{\boldsymbol{\psi}}_{I'}(\boldsymbol{r}) \rangle. \quad (13)$$

To address the question of the effective mass, we can perform variational calculations in the space of states obtained by translating a localized paired skyrmion $|\phi\rangle$ by all possible moiré lattice vectors. This defines an effective skyrmion hopping model leading to delocalized "Bloch skyrmions" and a Bloch dispersion, from which M_{pair} can be extracted. Note that this way of calculating the paired-skyrmion mass is completely different from the classical calculation of M_{pair} used to obtain the second equality of Eq. (7). The technical details of the skyrmion-plane-wave calculations, including generalizations involving symmetry-related skyrmions, are outlined in Appendix B of Ref. [54].

III. PSEUDOSPIN TEXTURES AT EVEN INTEGER FILLING

A. 1e skyrmions

Figure 3(a) shows the charge density of a $1e$ skyrmion relative to the translation-invariant $\nu = 0$ ground state. The Chern couplings J and λ can be controlled by tuning the effective one-body term and the chiral ratio, respectively. Since the Hamiltonian obeys particle-hole symmetry, adding holes instead of electrons leads to analogous results.

In the isotropic limit with $J = \lambda = 0$, the ground state can be any member of the $\mathrm{U}(2) \times \mathrm{U}(2)$ manifold described by independent choices of $\boldsymbol{n}_+$, $\boldsymbol{n}_-$. (Strictly speaking, the $|C| = 2$ ferromagnets are also ground states, but these do not allow for textures.) As verified numerically, the extra charge enters as a delocalized skyrmion solely in one of the Chern sectors, while the other sector remains unchanged. Hence, its properties are qualitatively the same as for spin skyrmions about the $\nu = 3$ QAH insulator (see Sec. IV). Consistent with the absence of anisotropies, the skyrmion expands as much as possible and is limited only by the finite simulation cell. This explains the slow convergence in Fig. 3(b) of the $1e$-skyrmion energy $E_{1e\ \mathrm{skyr}}$ (measured with respect to the $1e$-particle excitation E_{1e}) with the linear system dimension L, compared with other cases. Note that both $E_{1e\ \mathrm{skyr}}$ and E_{1e} are many-body energies that are computed self-consistently, and hence account for possible

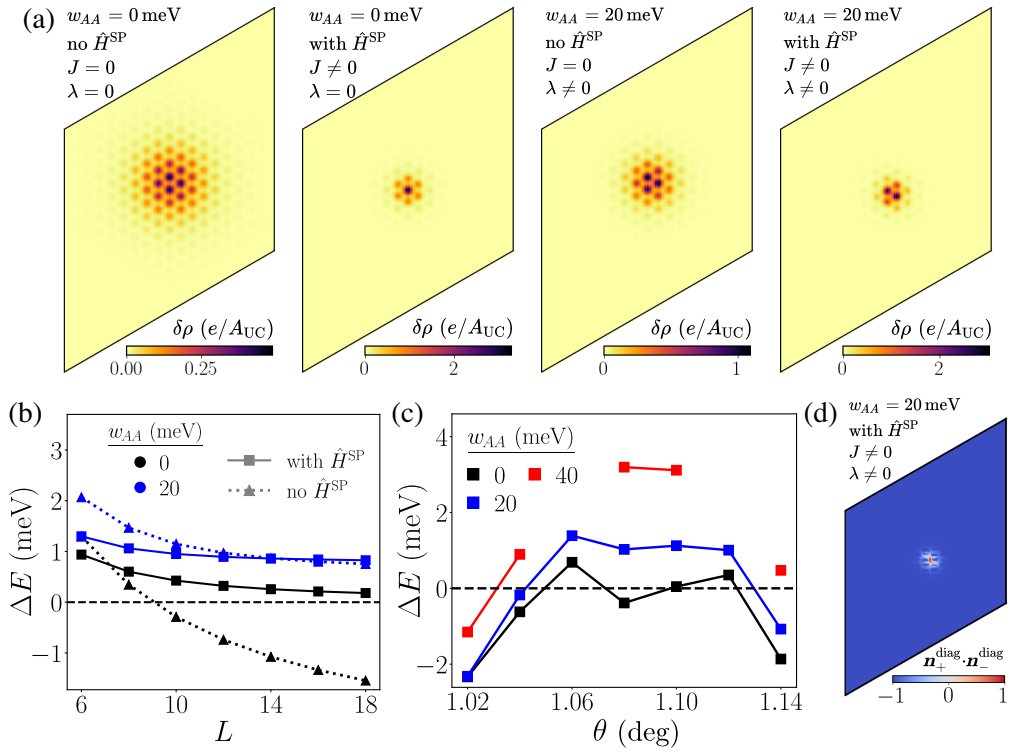

FIG. 3. Properties of $1e$ skyrmions (spinless $\nu = 0$). (a) Charge density $\delta\rho(\boldsymbol{r})$ of $1e$ skyrmions in the entire simulation cell relative to the $\nu = 0$ ground state. Panels show different combinations of turning on or off dispersion and achirality, which determine J and λ. Calculations performed on 18×18 systems at $\theta = 1.05°$. Textures manually translated to the center for clarity. (b) Relative energy $\Delta E = E_{1e\ \mathrm{skyr}} - E_{1e}$ of $1e$ skyrmions (compared to particle excitations) as a function of the system size. Both $E_{1e\ \mathrm{skyr}}$ and E_{1e} are computed self-consistently. Apart from the isotropic limit (black triangles), $1e$ skyrmions are not favored. (c) ΔE for different θ and w_{AA}. Dispersion is always included. System size is 11×11. Missing data points indicate parameters where HF is unable to find skyrmion solutions. (d) Local alignment of Chern pseudospins corresponding to the rightmost panel of (a). All calculations use the average scheme (see Appendix A in Ref. [54]).

reorganizations of the original $\nu = 0$ insulator induced by the added electron. Fitting to a power law $\Delta E(L) = \Delta E(\infty) + \alpha L^{-\gamma}$, we obtain $\Delta E(\infty) = -4.1$ meV, $\alpha = 18.3$ meV, and $\gamma = 0.68$. Note that the band gap at $\nu = 0$ depends only weakly on L since there is a direct gap at Γ_M. Hence, in the NLSM picture, the L dependence is expected to predominantly arise from the system size constraint on R_s which controls the interaction contribution to Eq. (4). Given that the gate screening length is comparable to the moiré length $d_{\mathrm{sc}} \simeq a^M$, one expects $\gamma > 1$ in the continuum limit for $R_s \gg a^M$. The discrepancy suggests that lattice corrections [the dotted patterns in Fig. 3(a) denote the AA-stacking regions] and finite-size effects have a quantitative impact here.

In the presence of anisotropies, the $1e$ skyrmions become finite sized. For example, in the chiral-nonflat limit with $J \neq 0, \lambda = 0$, the charge density is localized to within a few moiré lengths, leading to faster energy convergence with system size. This is consistent with the intuition from the NSLM, and the energetics of the skyrmion becomes significantly less favorable. The parent insulator is a member of the SU(2) family containing the KIVC and the valley Hall state (e.g., polarizing into KA and $K'A$ bands). The global net Chern polarization is less than $1/L^2$, consistent with the fact that the superexchange tunnels between opposite Chern sectors.

A similar story holds for the nonchiral-flat limit with $J = 0, \lambda \neq 0$, except the $\nu = 0$ insulator now interpolates between the KIVC and the valley-polarized state. This time, the added skyrmion is perfectly Chern polarized.

Including both perturbations, which is the case for realistic TBG, the symmetry reduces to the U(1) family of KIVC insulators, and the Chern polarization of the skyrmion is imperfect again. Figure 3(d) illustrates that the localized violation of Chern antialignment occurs at the same position as the charge-density modulation, confirming the skyrmionic nature of the added charge. In Fig. 3(c), we chart the relative energy of the skyrmions as a function of θ for different chiral ratios. For the average scheme, the $1e$ skyrmions are actually most costly near the magic angle where J is suppressed [compare with Fig. 2(b)]. This is despite the fact that artificially turning off J while keeping other parameters fixed improves the skyrmion energy significantly [Fig. 3(b)]. On the other hand, λ is largely constant as a function of θ. This suggests that the continuum description in terms of a small number of coupling parameters is not completely adequate.

The numerical results for ΔE in any plot such as Fig. 3(c) are generally expected to represent upper bounds for two reasons. First, our calculations are performed on finite system sizes L. In the thermodynamic limit $L \to \infty$, the skyrmions will have some ideal radius $R_s(\infty)$ set by the intrinsic properties of the BM model and interaction potential. Unless $L \gg R_s(\infty)$, the pseudospins in our calculation will experience some degree of frustration from the finite simulation cell, leading to an energy penalty. In addition, a larger L introduces a greater number of basis Bloch states which allows for smoother pseudospin rotations. Second, the restriction to Slater determinants in HF likely impacts skyrmions more than particlelike excitations. As shown in Sec. III D, skyrmions can gain a small delocalization energy by going beyond mean field and restoring the translation symmetry.

B. $2e$ skyrmions

Figure 4(a) shows the textured configurations when two electrons are added to the translation-invariant $\nu = 0$ ground state. As before, the Chern couplings J, λ can be controlled through the effective one-body term and the chiral ratio, respectively.

For $J = \lambda = 0$, the texture breaks moiré translation symmetry completely, but the charge density appears to spread throughout the system without a clear identification of one or two well-defined objects. Interestingly, the lowest-energy solution consists of both additional charges entering the same Chern sector, meaning that from a symmetry standpoint the situation will again be qualitatively similar to adding two charges to the QAH state. As shown in Fig. 4(b), the pseudospin alignment (note that one Chern sector has a constant pseudospin) rotates in a complicated fashion without reconstructing a new superlattice periodicity. However, in analogy to the case of SU(2)-invariant spin textures in Sec. IV, the inclusion of more doped electrons can result in a so-called "double-tetarton lattice" [51] with emergent periodicity if they all Chern polarize. The resulting pseudospins form an ordered pattern as shown in Figs. 12(a)–12(c).

In the chiral nonflat limit with $J \neq 0, \lambda = 0$, the charge density consists of a single smooth modulation with approximate circular symmetry. This is precisely an explicit realization of a paired $2e$ skyrmion: a skyrmion and an antiskyrmion with identical spatial profiles in the two Chern sectors exactly overlapping. This binding is induced by the superexchange J, as evidenced by the perfect antialignment of Chern pseudospins (and hence, $\hat{\mathcal{T}}'$ symmetry). In the absence of other perturbations, the paired skyrmions spread out and are limited only by the system size, leading to slow convergence in Fig. 4(c). Hence, the resulting physics controlling the texture is similar to that of the $1e$ skyrmion in the isotropic limit.

In the nonchiral-flat limit with $J = 0, \lambda \neq 0$, one may naively expect a similar paired skyrmion where the pseudospins are locked instead as $n_{+,z} = n_{-,z}$ and $\boldsymbol{n}_{+,xy} = -\boldsymbol{n}_{-,xy}$. However, this does not work as it leads to an electrically neutral object. The numerics reveal that both charges predominantly go into the same Chern sector. For small system sizes, the state closely resembles the double-tetarton lattice of the isotropic limit, which is reflected in the energetic trends in Fig. 4(c) for small L. For larger sizes, the lattice deforms such that the texture is better described by a nearby pair of $1e$ skyrmions. While this may be considered pairing

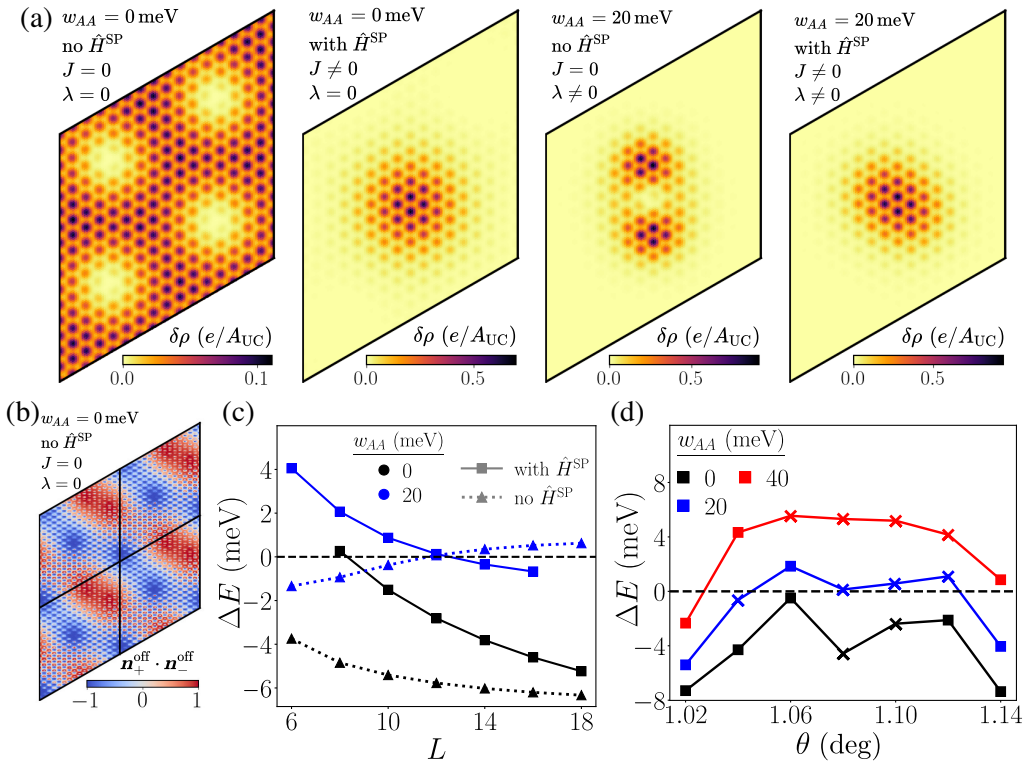

FIG. 4. Properties of $2e$ skyrmions (spinless $\nu = 0$). (a) Charge density $\delta\rho(\boldsymbol{r})$ of $2e$ skyrmions in the entire simulation cell relative to the $\nu = 0$ ground state. Panels show different combinations of turning on or off dispersion and achirality, which determine J and λ. Calculations performed on 16×16 systems at $\theta = 1.05°$. Textures manually translated to the center for clarity. (b) Local alignment of Chern pseudospins corresponding to the leftmost panel of (a). The system cell is duplicated three times for presentation. (c) Relative energy $\Delta E = E_{2e\ \mathrm{skyr}} - E_{2e}$ of $2e$ skyrmions (compared to adding two particle excitations) as a function of the system size. Both $E_{2e\ \mathrm{skyr}}$ and E_{2e} are computed self-consistently; $\Delta E < 0$ indicates that the $2e$ skyrmion is favored. (d) ΔE for different θ and w_{AA}. Dispersion is always included. Note that most of the solutions (indicated with crosses rather than squares) for $1.05° < \theta < 1.13°$ are not $\hat{\mathcal{T}}'$-symmetric paired skyrmions. System size is 11×11. All calculations use the average scheme (see Appendix A in Ref. [54]).

(actually, since $\Delta E > 0$, it is a metastable bound state that is unstable toward decaying into two particles), we reserve the term paired skyrmion for the $\hat{\mathcal{T}}'$-symmetric cases where a skyrmion and an antiskyrmion from opposite Chern sectors bind. It is noteworthy that ΔE increases as a function of L, bucking the trends of all other types of $1e$ and $2e$ skyrmions. This occurs because for $L \lesssim R_s(\infty)$, the constituent skyrmions are forced to strongly interact with each other in the confined system area and may therefore form a delocalized configuration with better energetics.

It is clear from Fig. 4(c) that reintroducing dispersion to the achiral-flat limit is favorable to the textures, which are once again paired skyrmions. The faster convergence of the relative energy with L is a hint that these paired skyrmions are now finite in size. This is clear from Fig. 5(a), which illustrates that increasing the chiral ratio not only reduces the skyrmion area, but also leads to an elliptical shape. As we discuss in Sec. II C, this could be anticipated from the NLSM analysis which predicts that the λ term penalizes the pseudospins when they antialign out of plane. This anisotropy is apparent in Figs. 5(b) and 5(c), where $n_{+,z}(\boldsymbol{r})$ has a much tighter profile than $n_{+,xy}(\boldsymbol{r})$. At mean-field level, the orientation of the n_z lobes is very soft, with distinct HF solutions differing by $\lesssim 10\mu$eV.

The energetic trends of the $2e$ skyrmions as a function of θ and w_{AA} are shown in Fig. 4(d). Note that specific to the average scheme, λ significantly exceeds J for a finite region of θ around the flat-band point. Consequently, in the range of approximately 1.05° to approximately 1.13°, the best textured solution has finite Chern polarization and breaks $\hat{\mathcal{T}}'$, and hence, is not a paired skyrmion.

Strain and substrate alignment represent two single-particle perturbations that are deleterious to the paired skyrmions, making them less energetically favorable and harder to find within HF. Strain significantly increases the kinetic bandwidth and is known to substantially degrade the gap of the KIVC at charge neutrality, eventually leading to a symmetric semimetal [60]. As shown in Fig. 6(a), strain of strength $\epsilon \lesssim 0.1\%$ is enough induce a positive relative energy ΔE for paired skyrmions. This should be interpreted in the context of STM studies which typically measure strains of 0.1%–0.7% [68,69,71]. A staggered sublattice potential $\Delta\sigma_z$ breaks $\hat{C}_{2z}$ and acts as a constant easy-axis Zeeman field with opposite direction in the two Chern

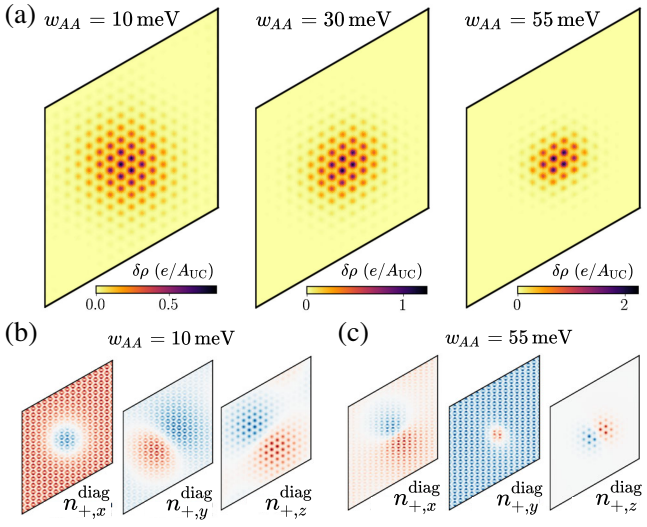

FIG. 5. Paired $2e$ skyrmions (spinless $\nu = 0$). (a) Charge density $\delta\rho(\boldsymbol{r})$ of paired skyrmions for different w_{AA}. (b),(c) Local pseudospin orientation in one Chern sector corresponding to the first and third panels of (a). Note the increasing degree of anisotropy and confinement for increasing chiral ratio. System size is 16×16 with the average scheme.

sectors, which deters smooth rotations in pseudospin space [Fig. 6(b)]. For Δ beyond a fraction of a meV, HF fails to stabilize paired skyrmions at all. In fact, if the coupling is strong enough, the mean-field ground state becomes a valley Hall state with no intervalley coherence [20]. On the other hand, increasing the strength of interactions tends to favor the paired skyrmions. This can be achieved by increasing the gate screening distance $d_{\rm sc}$ [Fig. 6(c)] or reducing the relative permittivity ϵ_r [Fig. 6(d)].

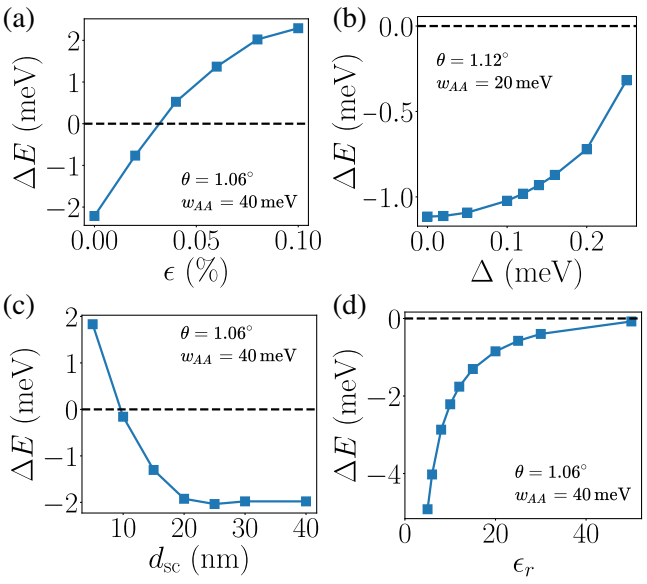

FIG. 6. Paired skyrmions and perturbations (spinless $\nu = 0$). Dependence of the relative energy of the paired skyrmion $\Delta E = E_{2e\ \rm skyr} - E_{2e}$ as a function of the (a) strain ratio ϵ, (b) substrate coupling Δ, (c) gate screening distance $d_{\rm sc}$, and (d) relative permittivity ϵ_r. System size is 13×13 with the graphene scheme. Qualitatively similar results are obtained for the other schemes.

C. Skyrmion composites and crystallization

By going beyond one or two particles, we can generate (metastable) higher skyrmion composites and skyrmion crystals. Figure 7(a) shows a typical configuration obtained by adding three electrons on top of $\nu = 0$, resulting in a $1e$ skyrmion (in the $C = +1$ sector) and a paired $2e$ skyrmion that position themselves apart due to Coulomb repulsion. This identification can be straightforwardly made by looking at the pseudospin orientation. On the other hand, adding four electrons can lead to a $\hat{\mathcal{T}}'$-symmetric clump of two paired skyrmions which arrange their n_z lobes in order to minimize the gradient cost [Fig. 7(b)]. For larger numbers of particles, the random initialization of the self-consistent HF loop tends to drive the system into local minima with complicated translation-symmetry-breaking patterns [Fig. 7(f)]. Such states are often well characterized by clumps or "trains" of paired skyrmions with suitably arranged pseudospin lobes punctuated by $1e$ skyrmions within the gaps. The prevalence of such motifs, even for large w_{AA} where particle-hole excitations are favorable, points to the robustness of skyrmions as well-defined localized excitations far away from the perturbative strong-coupling regime.

For intermediate dopings, the skyrmions can lose their individual identities and order into textured crystals. This is already shown in the isotropic limit for two added particles in Figs. 4(a) and 4(b), but it can occur even with anisotropies if the interskyrmion spacing becomes comparable with $R_s(\infty)$. For six extra particles, we can find a meron crystal where the lobes of the paired skyrmions lie on the honeycomb sites [Fig. 7(c), compare with Fig. 12(d)]. Figures 7(d) and 7(e) are examples of double-tetarton lattices with different emergent supercells.

D. Effective mass of paired skyrmions

A key prediction of the NLSM analysis is that paired skyrmions have a finite dispersion [22], which is crucial for generating a finite BKT energy scale E_c for superconductivity. In the NLSM framework, this generation of a finite mass is nontrivial, arising from the interplay between the superexchange J and the contrasting magnetic fields. An important question is how this picture holds up in the periodic moiré setting, where magnetic fields and flat bands are replaced by inhomogeneous Berry curvatures and interaction-renormalized dispersions. We address these issues using the effective hopping model described in Appendix B of Ref. [54], paying close attention to the dependence on the twist angle θ and subtraction scheme (the role of the subtraction is explained in Sec. II A and Appendix A of

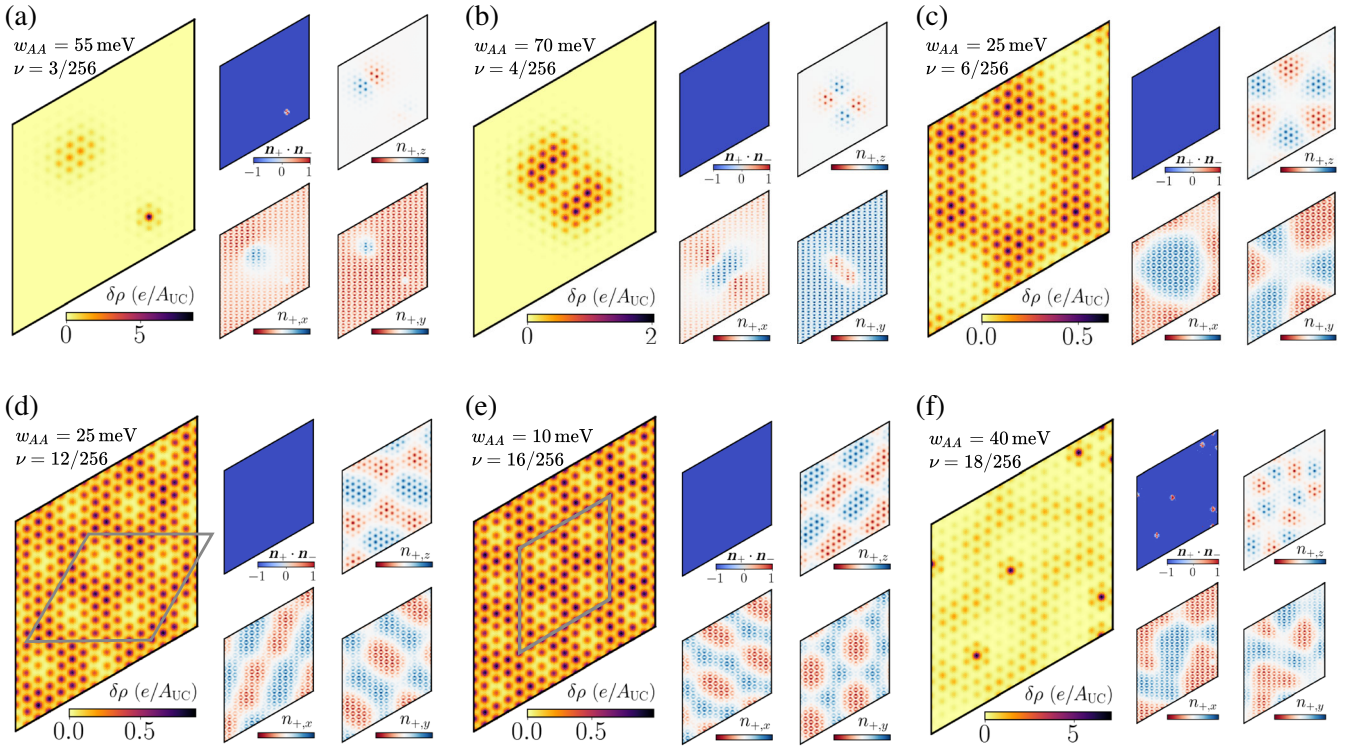

FIG. 7. Skyrmion composites and crystallization (spinless $\nu = 0$). Charge density $\delta\rho$, inter-Chern pseudospin alignment $\boldsymbol{n}_+ \cdot \boldsymbol{n}_-$, and pseudospin orientation $\boldsymbol{n}_+$ for different numbers of electrons above charge neutrality $\nu = 0$ in the spinless model. Emergent supercells for the double-tetarton lattice are highlighted in gray. All pseudospin densities are diagonal in microscopic layer or sublattice. System size is 16×16 with the average scheme.

Ref. [54]). Because of moiré translation invariance under $\hat{T}_{\boldsymbol{R}}$, our method is in essence a variational calculation of "Bloch skyrmions" $|\psi_{\boldsymbol{q}}\rangle = (1/L)\sum_{\boldsymbol{R}} e^{i\boldsymbol{q}\cdot\boldsymbol{R}}\hat{T}_{\boldsymbol{R}}|\phi\rangle$ based on a starting localized skyrmion $|\phi\rangle$ with an ideal pseudospin structure at the mean-field level. The required inputs are the matrix elements $\langle\phi|\hat{T}_{\boldsymbol{R}}|\phi\rangle, \langle\phi|\hat{H}\hat{T}_{\boldsymbol{R}}|\phi\rangle$ of $|\phi\rangle$ and its translated images.

In Figs. 8(a) and 8(b), we show the resulting band structure of $1e$ skyrmions and paired skyrmions, measured relative to the energy of the starting texture. The $1e$ skyrmion is characterized by a sharp peak at Γ_M and shallow minima near the zone boundaries (the positions of these features may change for larger w_{AA}, but the overall structure remains the same). Usually, a large number of overlaps and matrix elements beyond nearest neighbors needs to be computed to converge for a fixed set of parameters.

On the other hand, the paired skyrmions are robustly associated with a broad energy minimum at Γ_M and peaks at the zone corners. Typically, only matrix elements for distances $\lesssim 2a^M$ need to be computed to accurately describe the properties of the full hopping model. The skyrmion mass $M_{\rm pair}$, and hence, the BKT energy scale E_c, can be estimated by fitting a parabola to the band minimum. This typically leads to T_c of order 1 K. Figure 8(c) plots the convergence of E_c with system size L, which implies that the finite-size calculations here will typically underestimate the $L \to \infty$ results. As can be verified by checking nearest-neighbor overlaps, there is no "orthogonality catastrophe" for moiré translations—the spatially inhomogeneous part of a paired skyrmion is finite in size, and most regions of the HF state remain translation invariant.

Having established the basic properties of the hopping model for paired skyrmions, we now turn to details of the dependence of E_c on various parameters. The main motivation is to touch base with experiments which have observed a T_c dome as a function of the twist angle [41]. However, as we note in Sec. III B, there is a large window of θ centered at the magic angle where paired skyrmions cannot be found in the average scheme. The utility of this scheme is that J can be easily toggled by artificially turning off the kinetic Hamiltonian, but the drawback is that J therefore becomes substantially smaller than λ when the BM bands are flat, leading to a different type of $2e$ skyrmion. To address this issue, we consider now two alternative schemes which are not fine-tuned to have a vanishing superexchange.

Figure 8(d) charts the relative energy of the paired skyrmion as a function of θ and w_{AA} for the CN scheme. In contrast to Fig. 4(d), the paired skyrmions are energetically favored in an energy window centered on the magic

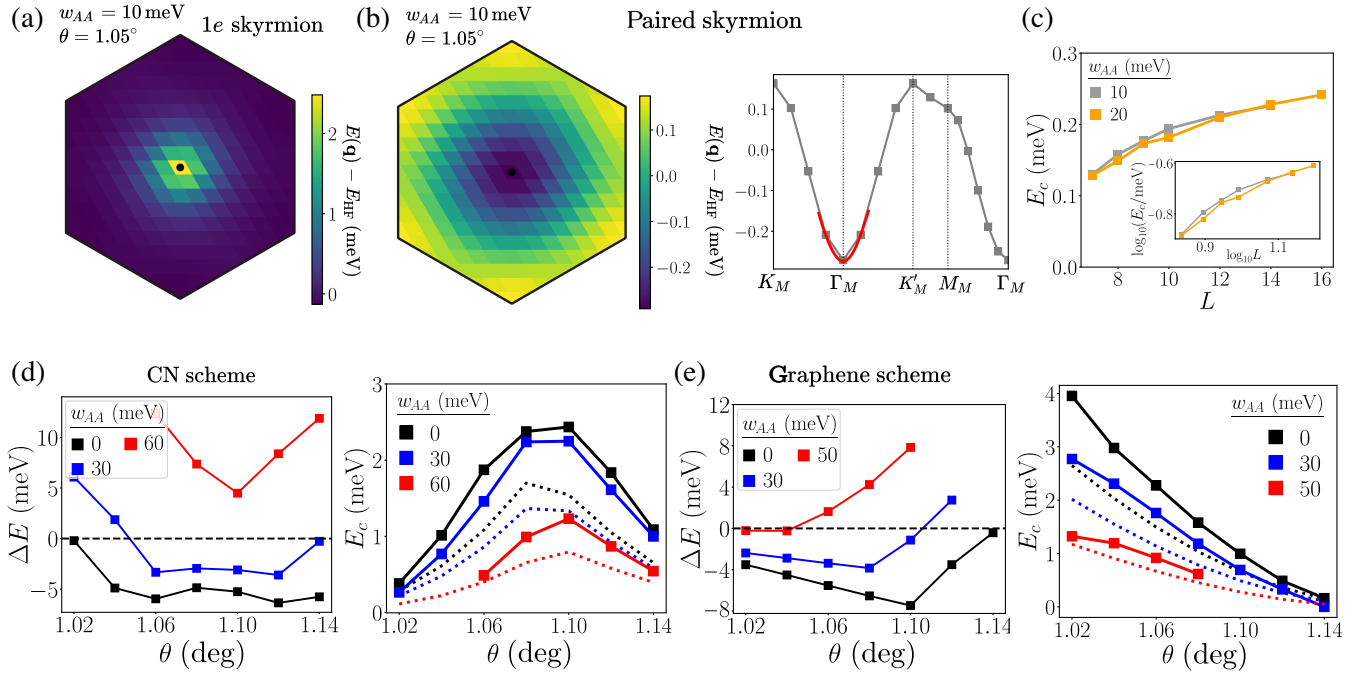

FIG. 8. Effective mass of paired skyrmions (spinless $\nu = 0$). (a),(b) Dispersion of 1e skyrmion and paired skyrmion, respectively, in the MBZ, obtained using an effective hopping model. Energy is measured relative to the localized HF solution. Black dot indicates Γ_M. For the paired skyrmion, we also show its band structure along a cut in the MBZ. Red line indicates the extraction of the effective mass. System size is 14×14 with the average scheme. (c) Convergence of the superconducting BKT scale $E_c = (\pi\hbar^2/2A_{\rm UC}M_{\rm pair})$ for the paired skyrmion with system size, in the average scheme. The effective mass $M_{\rm pair}$ is fitted to the minimum of the skyrmion dispersion. Inset shows log-log plot. (d) Left: paired-skyrmion energy $\Delta E = E_{2e\ \rm skyr} - E_{2e}$ relative to particle excitation as function of θ for different w_{AA} in the CN scheme. System size is 11×11. Right: E_c (solid) extracted from the skyrmion dispersion compared with the superexchange scale $E_J/2$ (dotted) computed directly from the properties of $\hat{H}$. (e) Same as (d) except using a graphene scheme.

angle. Again, ΔE has an inverted relation compared to J, which is plotted with dotted lines in the right panel. Note that paired skyrmions can be found up to $w_{AA} = 60$ meV for $L = 11$, which should improve with increasing system size. Looking at the hopping model results, E_c appears to qualitatively follow the same trends as J for the whole range of twist angles investigated, suggesting that the physical intuition from the NLSM maintains some level of validity in the lattice case. Notably, the CN scheme suggests that a skyrmion superconductor would have a T_c dome around the magic angle.

The graphene scheme in Fig. 8(e) paints a somewhat different picture—E_c monotonically increases in concert with J for decreasing twist angle. For smaller angles, the applicability of this calculation will be cut off by the fact that the parent insulator is no longer the ground state. Similarly, the paired skyrmions, at least for small chiral ratios, become less favorable compared to particle excitations. Hence, there are still possibilities for the hopping model results in the graphene scheme to be consistent with a T_c dome.

The stability of paired skyrmions in the CN, graphene, and average schemes is summarized in Fig. 9. Energetically favorable skyrmions can be found up to $w_{AA} \simeq 50$ meV for the right twist angles in the CN and graphene schemes (this is likely an underestimate when accounting for skyrmion delocalization and finite system size). Beyond this, metastable solutions are obtained for chiral ratios as large as $w_{AA} \simeq 65$ meV. Closer to realistic values of $w_{AA} \simeq 80$ meV, we find that HF is not able to converge to any paired-skyrmion states. In the average scheme, the paired skyrmions are energetically unfavorable close to the magic angle.

It is notable that different subtraction schemes lead to radically different behaviors in E_c. Indeed, we believe that this is one of the few cases where such a choice impacts a physical quantity in a qualitative way. Many theoretical studies focus primarily on the type of symmetry-breaking order [5,6,8,20,65,66,75–84]—all the schemes studied here lead to the KIVC, which requires only that $J, \lambda > 0$. On the other hand, we are interested in the θ dependence of E_c, which depends sensitively on the value of J itself.

The origin of this discrepancy can be understood by examining the effective dispersion $\hat{H}^{\rm SP}$ in more detail. As explained in Appendix A of Ref. [54], its matrix elements take the form

$$h^{\rm SP}(\boldsymbol{k}) = h^{\rm BM}(\boldsymbol{k}) + \frac{1}{2A}\sum_{\boldsymbol{q}} V_{\boldsymbol{q}} \Lambda_{\boldsymbol{q}}(\boldsymbol{k}) Q^0(\boldsymbol{k}+\boldsymbol{q})^T \Lambda^\dagger_{\boldsymbol{q}}(\boldsymbol{k}). \quad (14)$$

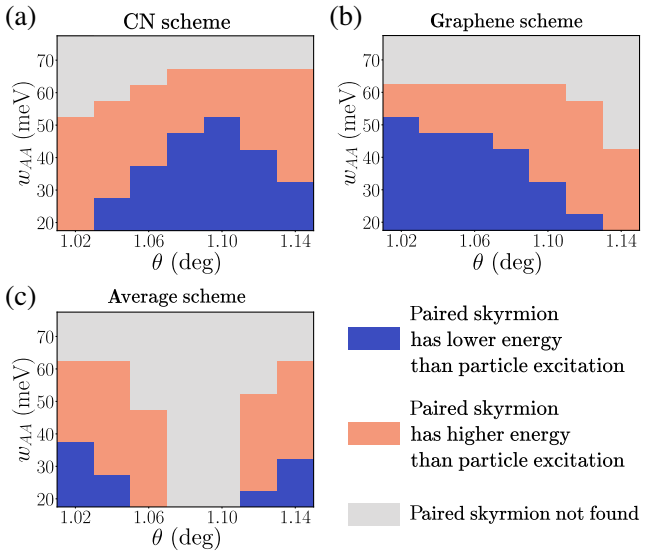

FIG. 9. Stability of paired skyrmions (spinless $\nu = 0$). (a) Phase diagram in the θ vs w_{AA} plane showing where paired skyrmions are energetically favorable (blue) or unfavorable (orange) compared to two particlelike excitations about the spinless $\nu = 0$ insulator. Gray indicates regions where HF fails to find a metastable paired-skyrmion solution. System size is 14×14 with the CN scheme. (b),(c) Same as (a) but with the graphene and average scheme.

J depends quadratically on the overall magnitude of h^{SP}. In the expression above, $P^0 = \frac{1}{2}(1 + Q^0)$ is the reference projector of the particular scheme. For the average scheme, $Q^0 = 0$ so that the only single-particle contributions (when the interaction terms are recast in strong-coupling form) arise from the kinetic piece h^{BM} which gets heavily suppressed at the magic angle.

P^0 for the CN scheme is constructed by occupying the valence bands of the BM Hamiltonian, while P^0 for the graphene scheme is built by filling the decoupled Dirac cones of each layer to the charge neutrality point and projecting to the central bands. An important clue is that both schemes qualitatively agree for θ above the magic angle. We focus on the states in the vicinity of the Dirac points for simplicity. For large angles, the Dirac cones of TBG are simply renormalized versions of those in decoupled graphene. In particular, we can calculate the behavior of the relative sublattice phase $\omega = \arg(u_{1A}/u_{1B})$ for the valence-band Bloch function as we traverse a small circle around a Dirac point. From a fixed starting point, ω will wind by 2π with some initial offset that agrees for both TBG and decoupled layers. As θ is reduced, the BM bands distort until we reach the magic-angle regime where the Dirac velocity vanishes and the bandwidth becomes tiny. Continuing past this point, the valence and conduction bands of TBG actually swap roles [85], which is reflected in an additional π offset in ω.

The crucial insight is that the filling of the CN projector tracks this band reversal, while the graphene projector is oblivious to this physics. Note that the second term of Eq. (14) represents the subtraction of the exchange gain for the filled bands of P^0. For the CN scheme, this is a positive contribution for the valence band of the BM model, which counteracts the negative contribution from the BM kinetic term itself. Therefore, the two parts of Eq. (14) tend to cancel each other out, leading to a dome at the magic angle when $h^{\mathrm{BM}}(\boldsymbol{k})$ becomes suppressed. For the graphene scheme, this destructive interference occurs above the magic angle. However, when the BM bands swap roles, the graphene projector does not follow, and hence, the two parts add constructively for smaller θ.

We reserve judgment on the matter of which scheme is most appropriate for capturing the physics in experimental TBG. Each choice has its own merits and justifications. The average scheme is the simplest and puts the strong-coupling hierarchy front and center. The graphene scheme aims to prevent additional renormalizations of the Dirac cones that have already been accounted for in the input value for the bare Dirac velocity. The CN scheme provides a base point (i.e., charge neutrality of the BM model) at which the BM kinetic energy is precisely the mean-field band structure. However, it is known to lead to incommensurate Kekulé spiral (IKS) order at extremely small strains for nonzero integer ν [20]. The microscopically correct answer is likely complicated and may differ based on the twist angle itself.

Since paired skyrmions also break TRS and all point group symmetries, a natural extension of the effective mass calculation is to include symmetry-related partners of the starting HF solution $|\phi\rangle$ in a "hybridization + hopping" model (see Appendix B in Ref. [54] for details). By restoring the symmetries, this would shed light on the internal structure of the quantum skyrmion, including the angular momentum of pairing. However, we find that an orthogonality catastrophe prevents feasibility of this method. Partners that are constructed from symmetries that do not leave the $\nu = 0$ KIVC invariant, such as $\hat{\mathcal{T}}$, have effectively vanishing overlaps with $|\phi\rangle$. This is not surprising, since these operators have a nontrivial action on the pseudospins even in the bulk of $|\phi\rangle$ away from the localized paired skyrmion. However, partners related by certain symmetries of the KIVC, such as $\hat{C}_3$, also have suppressed matrix elements and overlap with $|\phi\rangle$, leading to splittings $\lesssim 10^{-6}$ meV. Fundamentally, the reason is that the skyrmion texture is really a many-body pseudospin rotation of the parent insulator involving many particles, as evidenced by Figs. 5(b) and 5(c). Hence, the Hamiltonian, which involves only few-body terms, cannot effectively couple the different partners.

Before closing this subsection, we remark on the qualitative agreement shown in Figs. 8(d) and 8(e) between our effective hopping model and the NLSM, which is surprising given the stark differences in the two approaches. The NLSM utilizes a semiclassical continuum picture that involves relative deformations in the two Chern sectors, and

is insensitive to effects arising from the spatially modulated moiré potential. On the other hand, our variational Bloch skyrmions maintain perfect pseudospin antialignment even for nonzero $\boldsymbol{q}$, owing to the $\hat{\mathcal{T}}'$ symmetry of the mean-field solution $|\phi\rangle$. The effective hopping model operates in the tunneling regime, and highlights the discrete translation symmetry. It is possible that introducing deformations to the input localized skyrmion will improve the energetics and further renormalize the effective mass. Given the spatially extended and many-body nature of the pseudospin texturing, it is natural to expect that skyrmions possess many soft deformation directions. One can consider the following generalization of our calculation that would account for this. The Bloch skyrmions $|\psi_{\boldsymbol{q}}\rangle = (1/L)\sum_{\boldsymbol{R}} e^{i\boldsymbol{q}\cdot\boldsymbol{R}}\hat{T}_{\boldsymbol{R}}|\phi_{\boldsymbol{q}}\rangle$ are still constructed as plane-wave superpositions of a Slater determinant. However, the energetic optimization is performed on the final Bloch skyrmion energy (expressions for the relevant matrix elements are provided in Appendix B of Ref. [54]). Hence, the intermediate localized state $|\phi_{\boldsymbol{q}}\rangle$ is generally $\boldsymbol{q}$ dependent and not a self-consistent mean-field solution. This procedure is significantly more challenging to carry out since there is no self-consistency property to exploit, and $|\phi_{\boldsymbol{q}}\rangle$ generally involves a many-body reconstruction of the starting insulator. An alternative route is to introduce additional (higher-energy) states into the effective hopping model to allow for further variational freedom. For example, one could add skyrmion solutions centered at different locations in the unit cell to better sample the effective "skyrmion moiré potential." In the absence of such a computation, we believe that the effective hopping model currently provides the most microscopically concrete estimate of the effective mass. This is especially true in the physically relevant regime of intermediate chiral ratios κ, where the semiclassical intuition leveraged in the NLSM approach loses its justification due to factors like the increased band dispersion and Berry curvature modulation, and reduced skyrmion size. The fact that the diametrically opposite approaches agree so well is a good indication that the main features of the effective mass have been captured. The true physics presumably lies somewhere between the two limits.

E. Spinful KIVC at $|\nu| = 2$

We now reintroduce spin and turn to filling factors near $|\nu| = 2$ where the mean-field ground state is also a KIVC insulator (we show only the results for $\nu = +2$, but the situation at $\nu = -2$ can be inferred from PHS). A representative member of the spin-degenerate manifold of states arising from the approximate $\mathrm{SU}(2)_K \times \mathrm{SU}(2)_{K'}$ symmetry consists of fully filling the spin-↑ flat bands while forming a spinless KIVC in the (minority) spin-↓ subspace. We concentrate on pseudospin skyrmions by enforcing collinear spins.

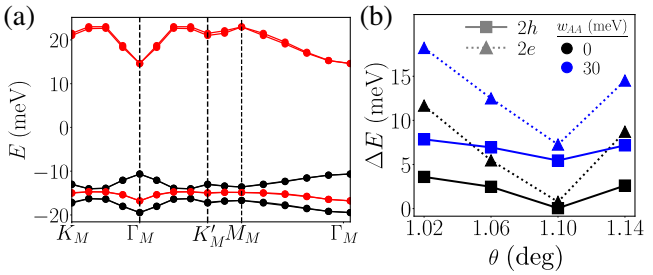

FIG. 10. Paired skyrmions (spinful $\nu = +2$). (a) Hartree-Fock dispersion of spin-polarized KIVC insulator at $\nu = +2$. Red (black) indicates minority (majority) spin carrier. System size is 24×24 with $\theta = 1.06°$. (b) Relative energy $\Delta E = E_{2e(h)\ \mathrm{skyr}} - E_{2e(h)}$ of $\hat{\mathcal{T}}'$-symmetric paired $2e$ and $2h$ skyrmions about $\nu = +2$. Note the sharp minimum of unfilled band at Γ_M. System size is 11×11 with the CN scheme.

Paired skyrmions can be constructed as before by treating the majority spin bands as spectator bands and performing nontrivial pseudospin rotations in the half-filled minority spin bands, but there are complications compared with the spinless neutrality case. First, the NLSM parameters J, λ reflect the relevant energy scales at the neutrality point of the strong-coupling Hamiltonian. However, the starting insulator now contains additional majority carriers, which impacts the effective energetics of the minority subspace. Second, this additional interaction renormalization enters in a particle-hole asymmetric way. Generally, the bands away from neutrality have a significantly enhanced bandwidth with a prominent extremum at Γ_M [86,87] [Fig. 10(a)], which disfavors skyrmions because they are built from momentum states throughout the MBZ. Third, the edge of the majority spin bands can lie inside the minority band gap which reduces the gap to particle-hole excitations. On the other hand, a pseudospin skyrmion cannot be formed by adding holes to a completely filled spin sector.

These considerations are reflected in the HF calculations in Fig. 10(b) at $\nu = +2$, showing that paired $2e$ skyrmions on the electron-doped side are more expensive than the paired $2h$ skyrmions on the hole-doped side. Overall, the relative energies ΔE are less favorable than the results at charge neutrality.

IV. SPIN TEXTURES AT $|\nu| = 3$

The physical intuition and considerations behind skyrmions in Sec. III can also be applied to odd-integer fillings. In this section, we briefly discuss textures near $\nu = +3$ that arise from doping the Chern, spin, and valley-polarized QAHI (the results at $\nu = -3$ can be found from particle-hole symmetry about neutrality). The situation here is significantly simpler because of the $\mathrm{SU}(2)_S$ spin-rotation symmetry that holds independent of the presence of dispersion or deviation from the chiral limit. Furthermore, the

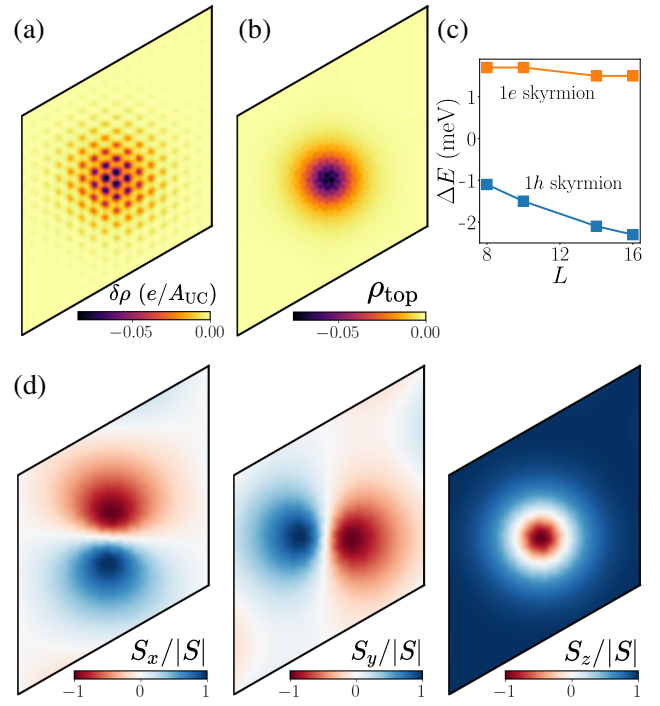

FIG. 11. Spin skyrmions about QAH (spinful $\nu = +3$). (a) Charge density of a single hole about the $\nu = +3$ QAH state. (b) Topological density ρ_{top} computed from the spatial spin configuration of (a). (c) Energy of single-electron and hole skyrmions $\Delta E = E_{1e(h)\text{skyr}} - E_{1e(h)}$ (relative to a particlelike electron or hole excitation) as a function of system size L. (d) Local spin orientation $\boldsymbol{S}(\boldsymbol{r})/|\boldsymbol{S}(\boldsymbol{r})|$ corresponding to the skyrmion in (a). The spins are rotated so that the state has a net polarization along z. System size is 16×16 with the graphene scheme.

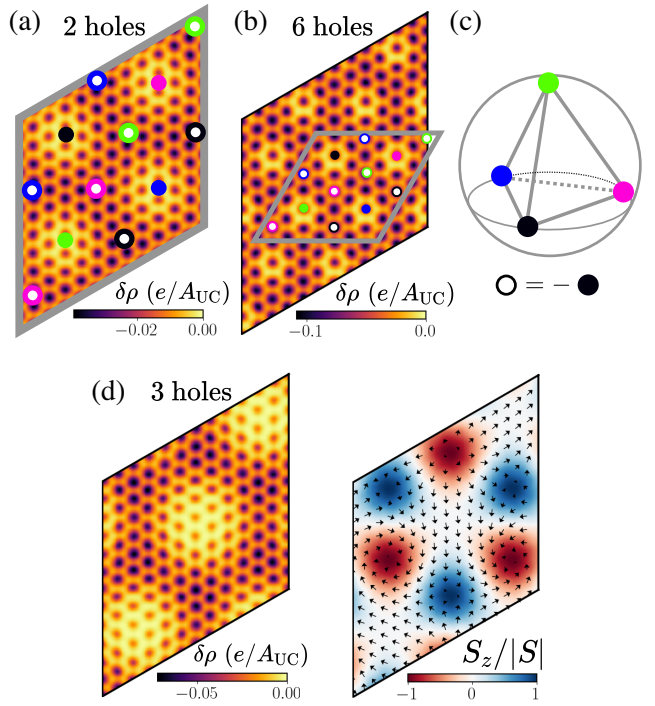

FIG. 12. Spin skyrmion crystallization about QAH (spinful $\nu = +3$). (a),(b) Charge density when adding two and six holes, respectively. Gray parallelogram indicates the supercell. (c) In the double-tetarton lattices of (a),(b), the spins at particular positions (anti) align along the corners of a tetrahedron in spin space. (d) Charge and z component of local spin orientation when adding three holes, leading to a meron lattice. System size is 12×12 with the graphene scheme.

starting insulator is easy axis in valley space. The low-energy charged topological excitations are then expected to be spin skyrmions [36,37,51] in the partially filled Chern sector without any texturing in the fully filled Chern sector.

In Fig. 11, we compute the properties of $1h$ and $1e$ skyrmions by relaxing the spin collinearity constraint in our HF calculations. In a similar fashion to isotropic $1e$ skyrmions in Fig. 3(a), the change in charge density is roughly circularly symmetric with moiré-periodic modulations on the AA-stacking regions. The local spin orientation is consistent with the hallmark features of an SU(2)-symmetric skyrmion. Indeed, the calculation of the topological density ρ_{top} (in spin space) confirms the topological origin of the excitation. Unlike in QHFM, there is no explicit Zeeman field, meaning that the skyrmion expands to fill the available system size to minimize the Coulomb energy. This is reflected in the slow convergence of ΔE with L. There is a clear asymmetry between adding holes and electrons because the interaction-renormalized band structure [86–91] at finite integer fillings strongly breaks particle-hole symmetry [see Fig. 10(a)].

Just as in Sec. III C, doping additional charges leads to the formation of various skyrmion crystals. The unit cell of the double-tetarton lattice [51] contains two charges with an intricate spin pattern illustrated in Figs. 12(a) and 12(c). An alternative configuration is the meron crystal whose unit cell is associated with a charge of $3e$ [Fig. 12(d)]. Computations on system sizes and dopings where both options can be stabilized are required to numerically determine the energetically preferred lattice. It has also been proposed that applying a Zeeman field will enrich the possible set of phases [51].

V. DISCUSSION

In closing, we consider various generalizations and extensions of the work presented above, comment on the possibility of experimentally observing skyrmion physics, and critically assess the implications of our work for the proposed skyrmion-driven mechanism for superconductivity in TBG.

A. More general skyrmions

In this work, motivated by our focus on particular aspects of physics in TBG, we impose restrictions on the directions

in flavor space that the skyrmions are allowed to rotate in. The strong-coupling insulators at different integer ν are all Chern ferromagnets, and starting from the fully symmetric limit, one can consider more general skyrmions where the only constraint is that locally the state is polarized within the Chern sectors. For instance, starting from the $|\nu| = +3$ QAHI, it is possible to form a texture in both spin and pseudospin to create an "entangled" skyrmion, akin to what happens at $|\nu| = 1$ in the zeroth LL of monolayer graphene [92]. With the full Hamiltonian, pseudospin rotations will be gapped since the QAHI is easy axis, while spin rotations remain low energy due to the $\mathrm{SU}(2)_S$ symmetry.

These considerations can be generalized to any integer filling. Starting from a generalized ferromagnetic insulator with $\tilde{\nu}_C$ filled bands in Chern sector C, the local flavor configuration is parametrized by two matrix spinors $f_C(\boldsymbol{r})$ living in Grassmannian projective spaces [93]

$$f_C(\boldsymbol{r}) \in \frac{\mathrm{SU}(4)}{\mathrm{SU}(\tilde{\nu}_C) \times \mathrm{SU}(4-\tilde{\nu}_C) \times \mathrm{U}(1)}, \tag{15}$$

where $\tilde{\nu}_+ + \tilde{\nu}_- = \nu$. The factors in the normal subgroup represent unitary rotations in within the filled bands, unfilled bands, and the phase difference between the filled and unfilled bands, respectively. The presence of four flavors and two spinors leads to a large manifold of skyrmions. From the discussion in Sec. II B, the leading corrections from the $\mathrm{U}(4) \times \mathrm{U}(4)$ limit will be anistropic couplings between the spinors, while additional single-particle perturbations such as substrate coupling may manifest as anisotropic fields. The relevant space of textures will be dictated by the energetics at a given filling.

The ground state in the spinful model at charge neutrality is the spin-unpolarized KIVC [5]

$$Q_{\mathrm{KIVC}} = \sigma_y(\tau_+ V + \tau_- V^\dagger), \tag{16}$$

where $V = e^{i\phi} e^{i(\varphi/2)\boldsymbol{m}\cdot\boldsymbol{s}}$ and $\tau_\pm = \frac{1}{2}(\tau_x \pm i\tau_y)$. This represents two copies of the spinless version in Eq. (3) with spin projections $\pm\boldsymbol{m}$ and IVC phases $\phi \pm (\varphi/2)$ (the relative phase φ is set by intervalley Hund's terms). Equivalently, we have four Chern pseudospins $\boldsymbol{n}_{C,s}$ where s indicates the projection of the spin along $\boldsymbol{m}$. Consider doping two electrons. Forming a paired skyrmion in one of the spin sectors in the usual way can be understood using the analysis of Sec. III. Attempting to rotate in spin space will either lead to Pauli blocking or the loss of antiferromagnetic exchange J, which justifies our restriction to pseudospin textures in Sec. III. Similar conclusions can be reached for the spin-polarized KIVC insulator at $|\nu| = 2$, though we cannot rule out the majority spin being nontrivially involved if it is the closest filled band to the chemical potential.

B. Disorder

The effects of disorder on skyrmions have been treated previously in the quantum Hall context [94–98]. A strong and smooth disorder potential can drive the system into a spin glass. We note that all the strong-coupling insulators of interest in this work violate TRS, and hence, ordinary impurities cannot directly couple to the symmetry-breaking order as a random field. Isolated charged impurities are expected to pin individual skyrmions as well as spin texture lattices, which may aid in their detection as we discuss in the following subsection. TBG can also harbor more subtle forms of disorder. For the QAHI, modulations in the magnitude and sign of the sublattice coupling Δ can lead to the enforced nucleation of domain walls, including ones which separate regions with opposite Chern number [46]. These would interrupt the propagation and crystallization of spin skyrmions. Twist-angle inhomogeneity [99], which is pervasive in experimental samples [68–71,100], is notoriously difficult to model, and its theoretical impact on the correlated insulators at integer fillings is still beyond quantitative characterization. For sufficiently long-wavelength fluctuations, the properties of the skyrmions (e.g., the effective masses) are likely to depend on the local twist angle.

C. Detecting skyrmions

The presence of spin textures about the QAHI at $\nu = +3$ could be detected by measuring the degradation of magnetization for small dopings, e.g., through NMR measurements [101], nitrogen-vacancy center magnetometry, or using a superconducting quantum-interference device [13]. Individual spin skyrmions involve a large number of spin flips, and the spin texture lattices of Fig. 12 are close to completely spin unpolarized. However, there is an orbital contribution from the spontaneous Chern polarization which is likely larger [13]. A more direct probe would be spin-resolved STM near impurity sites that could pin a localized skyrmion.

Measuring pseudospin textures at even integer filling is trickier since experimental techniques are not able to directly couple to the valley degree of freedom. IVC generally leads to $\sqrt{3} \times \sqrt{3}$ spatial order at the microscopic graphene scale, but the $\hat{\mathcal{T}}'$ symmetry of the KIVC insulator means that it does not exhibit a Kekulé density distortion (KD) [102,103]. Paired skyrmions preserve $\hat{\mathcal{T}}'$ and hence do not give rise to KD [103]. They may still leave a dipole-shaped fingerprint in sublattice polarization within regions where the state is locally in the valley Hall configuration, i.e., pseudospins antialigned and pointing along the z axis [Fig. 5(c)], but this is likely a faint signature since away from the chiral limit the Chern basis is only partially sublattice polarized. On the other hand, $1e$ skyrmions are tightly localized within a few moiré lengths and give rise to a spatially varying KD when pinned by charged impurities.

KD has been observed in the related context of QHFM within the lowest LL of monolayer graphene [104–106], including the imaging of an individual valley skyrmion [105]. We caution that KD in TBG has also been predicted for IKS order in the presence of a small amount of strain [20,103].

D. Skyrmion superconductivity

We finally turn to the implications of our work for skyrmion superconductivity. First, note that two important factors controlling the feasibility of this proposed mechanism are the stability of paired skyrmions (i.e., relative energy ΔE compared to particle excitations) and their effective masses. In general, we can conclude that paired skyrmions are especially favored close to the strongly interacting isotropic limit. The realistic value of w_{AA} lies in the range 55–90 meV (i.e., $\kappa \simeq 0.5$–0.8), and we find only paired skyrmions in the lower range of these values (Fig. 9). We note that a mechanism has been proposed that might drive a downward renormalization of the chiral ratio κ [9]. We note also that large skyrmions, which are relatively classical and relevant for small w_{AA}, are likely to be well captured in our mean-field treatment. However, for larger w_{AA}, the paired skyrmions become smaller and quantization effects are more important, and fluctuations can be more significant. In this regime, the mean-field result is really only an upper bound on the skyrmion energy, which could be lowered by fluctuations, which are not expected to substantially affect the single-particle excitations.

Enhancing interactions by suppressing screening, either through increasing the gate distance d_{sc} or decreasing the permittivity ϵ_r, also favors skyrmions (Fig. 6). However, this observation makes the superconducting domes that persist in Refs. [42–45] upon reducing the interaction strength difficult to reconcile with a topological mechanism. In these experiments, the insulators at integer ν, from which the skyrmions would be seeded, disappear with increasing screening. The superconducting region can also straddle the integers where the BKT transition temperature from Eq. (7) seemingly vanishes. Substrate coupling rapidly destroys pseudospin skyrmions, consistent with the absence of superconductivity in aligned samples [11,12]. This topological mechanism would not be effective in other moiré platforms that lack $\hat{C}_{2z}$ symmetry [22,107–110]. Strain takes the system away from the strong-coupling regime and similarly disfavors skyrmions: For instance, the parent insulator has been predicted to give way to a symmetric semimetal at charge neutrality or an IKS at nonzero integer fillings [20,60]. Hence, the general expectation from our work and from these experimental observations is that skyrmion superconductivity is most likely to emerge in "pristine" samples with minimal screening.

The question of effective masses [and hence, T_c via (Eq. (7)] is more subtle. We demonstrate that the dependence of the BKT transition scale E_c on θ is rather sensitive to precise details of how electron interactions are incorporated. Without further external inputs, e.g., from detailed *ab initio* studies or spectroscopic probes of the band structure over a range of twist angles, it is difficult to make quantitative contact with experiments such as Ref. [41] which show a dome in T_c near the magic angle. Any comparison would also inevitably be complicated by the presence of confounding variables such as twist-angle disorder [100] which are difficult to fully characterize, let alone control. However, what we can reliably distill from our numerical study is that paired skyrmions can in principle emerge with a sufficient mass to support an estimate of $T_c \lesssim 5$ K that is comparable to experimentally observed values. Both the CN and graphene schemes are able to support a nonvanishing superfluid velocity at the magic angle, and the fragility of the parent-correlated insulators to deviations of θ will tend to also reduce the strength of skyrmion superconductivity away from this regime.

The discussion above focuses primarily on a "BEC-like" limit of skyrmion superconductivity, where the binding is present already in the dilute limit; this is the regime primarily accessed in this work. An intriguing alternative possibility is a more BCS-like picture, where skyrmions, while unstable at low density, nevertheless become favored and paired at finite density. We note that Ref. [23], which studies skyrmion superconductivity in the Landau level limit, found superconductivity in the doped case, even in the absence of a pairing gap at zero doping.

Another potential challenge to the applicability of the skyrmion mechanism to TBG lies in the fact that superconductivity is most frequently observed near $\nu = -2$ on the side away from charge neutrality. On the other hand, our numerics show that paired skyrmions are relatively harder to stabilize at $|\nu| = 2$ compared to $\nu = 0$ [Fig. 10(b)]. Furthermore, the skyrmions are more disfavored when doping in the direction away from charge neutrality. This latter observation can be explained by the increased dispersion due to the interaction renormalization from the extra filled bands [Fig. 10(a)], and has been argued to be consistent with the asymmetry of the Landau fans [86].

We cannot rule out a scenario where skyrmion superconductivity is operative in only a subset of samples, for instance, the device studied in Ref. [4] which is nominally nonaligned with hexagonal boron nitride and exhibits a remarkably large number of correlated insulators and superconducting domes, including near neutrality. Another moiré material where the skyrmion mechanism may be a plausible explanation of superconductivity is mirror-symmetric magic-angle twisted trilayer graphene (TTG), which is closely related to TBG but has a somewhat larger value for the magic angle [111]. Interestingly, the superconductor in TTG is observed to have a very short coherence length [112], and an associated pseudogap regime [113]. Partly because of this, Refs. [112,113]

suggested that part of the TTG superconducting dome is in the BEC regime. Skyrmion pairing is a natural way to get preformed charge-2e bosons, and is at least known to give rise to superconductivity in the chiral limit of TBG [23]. It is therefore worthwhile to investigate whether this mechanism can explain at least a subset of the experimental observations in TTG.

In summary, our work provides clear evidence that the formation and pairing of skyrmions can indeed occur in microscopically faithful treatments of TBG, thereby illustrating that a purely electronic "topological" Cooper pairing mechanism can operate away from the exactly solvable limit without leveraging any approximate sigma-model description. However, despite this in-principle demonstration of the feasibility of a novel pairing mechanism, we cannot on the basis of present evidence definitively attribute superconductivity in TBG to this mechanism. This is highlighted by the difficulty in reconciling the deleterious effect of variations in strain and interaction strength and deviation from the chiral limit on the stability of skyrmions with the apparent robustness of superconductivity to such effects. Despite this, the uncertainty of various microscopic parameters and the mean-field nature of our study leave open a real possibility that a skyrmionic mechanism may ultimately survive these challenges. Further work, especially involving numerical approaches that can capture fluctuations beyond the mean-field level, is clearly warranted, as is the exploration of new regimes and systems where skyrmion pairing may be more favored and the identification of new probes that can directly interrogate the nature of the pairing "glue" in TBG.

ACKNOWLEDGMENTS

We thank Andrei Bernevig, Shubhayu Chatterjee, Eslam Khalaf, Ashvin Vishwanath, and Michael Zaletel for discussions. We are grateful to the authors of Refs. [114,115] for sharing advance copies of their preprints. G. W. acknowledges NCCR MARVEL funding from the Swiss National Science Foundation. N. B. is supported by a senior postdoctoral research fellowship of the Flanders Research Foundation. We acknowledge support from the European Research Council under the European Union Horizon 2020 Research and Innovation Programme, Grant Agreement No. 804213-TMCS and from EPSRC Grant No. EP/S020527/1. Statement of compliance with EPSRC policy framework on research data: This publication is theoretical work that does not require supporting research data.

Note added.—A preprint Ref. [114] that appeared in the same arXiv posting as ours performs a complementary analysis of spin 1e-skyrmion formation in the limit of small skyrmion size. In this regime, skyrmions may be viewed as "spin polarons" consisting of a charged electron or hole bound to a single spin-flip particle-hole pair excitation. Shortly afterward, Ref. [115] appeared, which studies singly charged trions in the BM model with all flavors.

[1] Y. Cao, V. Fatemi, A. Demir, S. Fang, S. L. Tomarken, J. Y. Luo, J. D. Sanchez-Yamagishi, K. Watanabe, T. Taniguchi, E. Kaxiras, R. C. Ashoori, and P. Jarillo-Herrero, *Correlated Insulator Behaviour at Half-Filling in Magic-Angle Graphene Superlattices*, Nature (London) **556**, 80 (2018).

[2] Y. Cao, V. Fatemi, S. Fang, K. Watanabe, T. Taniguchi, E. Kaxiras, and P. Jarillo-Herrero, *Unconventional Superconductivity in Magic-Angle Graphene Superlattices*, Nature (London) **556**, 43 (2018).

[3] M. Yankowitz, S. Chen, H. Polshyn, Y. Zhang, K. Watanabe, T. Taniguchi, D. Graf, A. F. Young, and C. R. Dean, *Tuning Superconductivity in Twisted Bilayer Graphene*, Science **363**, 1059 (2019).

[4] X. Lu, P. Stepanov, W. Yang, M. Xie, M. A. Aamir, I. Das, C. Urgell, K. Watanabe, T. Taniguchi, G. Zhang, A. Bachtold, A. H. MacDonald, and D. K. Efetov, *Superconductors, Orbital Magnets and Correlated States in Magic-Angle Bilayer Graphene*, Nature (London) **574**, 653 (2019).

[5] N. Bultinck, E. Khalaf, S. Liu, S. Chatterjee, A. Vishwanath, and M. P. Zaletel, *Ground State and Hidden Symmetry of Magic-Angle Graphene at Even Integer Filling*, Phys. Rev. X **10**, 031034 (2020).

[6] J. Kang and O. Vafek, *Strong Coupling Phases of Partially Filled Twisted Bilayer Graphene Narrow Bands*, Phys. Rev. Lett. **122**, 246401 (2019).

[7] B. A. Bernevig, Z.-D. Song, N. Regnault, and B. Lian, *Twisted Bilayer Graphene. III. Interacting Hamiltonian and Exact Symmetries*, Phys. Rev. B **103**, 205413 (2021).

[8] B. Lian, Z.-D. Song, N. Regnault, D. K. Efetov, A. Yazdani, and B. A. Bernevig, *Twisted Bilayer Graphene. IV. Exact Insulator Ground States and Phase Diagram*, Phys. Rev. B **103**, 205414 (2021).

[9] O. Vafek and J. Kang, *Renormalization Group Study of Hidden Symmetry in Twisted Bilayer Graphene with Coulomb Interactions*, Phys. Rev. Lett. **125**, 257602 (2020).

[10] S. M. Girvin, *The Quantum Hall Effect: Novel Excitations and Broken Symmetries*, in *Aspects topologiques de la physique en basse dimension. Topological Aspects of Low Dimensional Systems* (Springer, New York, 1999), pp. 53–175.

[11] A. L. Sharpe, E. J. Fox, A. W. Barnard, J. Finney, K. Watanabe, T. Taniguchi, M. A. Kastner, and D. Goldhaber-Gordon, *Emergent Ferromagnetism near Three-Quarters Filling in Twisted Bilayer Graphene*, Science **365**, 605 (2019).

[12] M. Serlin, C. L. Tschirhart, H. Polshyn, Y. Zhang, J. Zhu, K. Watanabe, T. Taniguchi, L. Balents, and A. F. Young, *Intrinsic Quantized Anomalous Hall Effect in a Moiré Heterostructure*, Science **367**, 900 (2020).

[13] C. L. Tschirhart, M. Serlin, H. Polshyn, A. Shragai, Z. Xia, J. Zhu, Y. Zhang, K. Watanabe, T. Taniguchi, M. E. Huber,

and A. F. Young, *Imaging Orbital Ferromagnetism in a Moiré Chern Insulator*, Science **372**, 1323 (2021).
[14] Y. Saito, J. Ge, L. Rademaker, K. Watanabe, T. Taniguchi, D. A. Abanin, and A. F. Young, *Hofstadter Subband Ferromagnetism and Symmetry-Broken Chern Insulators in Twisted Bilayer Graphene*, Nat. Phys. **17**, 478 (2021).
[15] J. M. Park, Y. Cao, K. Watanabe, T. Taniguchi, and P. Jarillo-Herrero, *Flavour Hund's Coupling, Chern Gaps and Charge Diffusivity in Moiré Graphene*, Nature (London) **592**, 43 (2021).
[16] I. Das, X. Lu, J. Herzog-Arbeitman, Z.-D. Song, K. Watanabe, T. Taniguchi, B. A. Bernevig, and D. K. Efetov, *Symmetry-Broken Chern Insulators and Rashba-like Landau-Level Crossings in Magic-Angle Bilayer Graphene*, Nat. Phys. **17**, 710 (2021).
[17] P. Stepanov, M. Xie, T. Taniguchi, K. Watanabe, X. Lu, A. H. MacDonald, B. A. Bernevig, and D. K. Efetov, *Competing Zero-Field Chern Insulators in Superconducting Twisted Bilayer Graphene*, Phys. Rev. Lett. **127**, 197701 (2021).
[18] K. P. Nuckolls, M. Oh, D. Wong, B. Lian, K. Watanabe, T. Taniguchi, B. A. Bernevig, and A. Yazdani, *Strongly Correlated Chern Insulators in Magic-Angle Twisted Bilayer Graphene*, Nature (London) **588**, 610 (2020).
[19] S. Wu, Z. Zhang, K. Watanabe, T. Taniguchi, and E. Y. Andrei, *Chern Insulators, van Hove Singularities and Topological Flat Bands in Magic-Angle Twisted Bilayer Graphene*, Nat. Mater. **20**, 488 (2021).
[20] Y. H. Kwan, G. Wagner, T. Soejima, M. P. Zaletel, S. H. Simon, S. A. Parameswaran, and N. Bultinck, *Kekulé Spiral Order at All Nonzero Integer Fillings in Twisted Bilayer Graphene*, Phys. Rev. X **11**, 041063 (2021).
[21] G. Wagner, Y. H. Kwan, N. Bultinck, S. H. Simon, and S. A. Parameswaran, *Global Phase Diagram of Twisted Bilayer Graphene above t_c*, Phys. Rev. Lett. **128**, 156401 (2022).
[22] E. Khalaf, S. Chatterjee, N. Bultinck, M. P. Zaletel, and A. Vishwanath, *Charged Skyrmions and Topological Origin of Superconductivity in Magic-Angle Graphene*, Sci. Adv. **7**, eabf5299 (2021).
[23] S. Chatterjee, M. Ippoliti, and M. P. Zaletel, *Skyrmion Superconductivity: DMRG Evidence for a Topological Route to Superconductivity*, arXiv:2010.01144.
[24] M. Christos, S. Sachdev, and M. S. Scheurer, *Superconductivity, Correlated Insulators, and Wess-Zumino-Witten Terms in Twisted Bilayer Graphene*, Proc. Natl. Acad. Sci. U.S.A. **117**, 29543 (2020).
[25] E. Khalaf, P. Ledwith, and A. Vishwanath, *Symmetry Constraints on Superconductivity in Twisted Bilayer Graphene: Fractional Vortices,* 4*e Condensates or Non-Unitary Pairing*, Phys. Rev. B **105**, 224508 (2022).
[26] D. Jing, A. C. Tyner, and P. Goswami, *Mechanism of Skyrmion Condensation and Pairing for Twisted Bi-Layer Graphene*, Phys. Rev. B **105**, 184505 (2022).
[27] F. Wu and S. Das Sarma, *Collective Excitations of Quantum Anomalous Hall Ferromagnets in Twisted Bilayer Graphene*, Phys. Rev. Lett. **124**, 046403 (2020).
[28] Y. H. Kwan, Y. Hu, S. H. Simon, and S. A. Parameswaran, *Exciton Band Topology in Spontaneous Quantum Anomalous Hall Insulators: Applications to Twisted Bilayer Graphene*, Phys. Rev. Lett. **126**, 137601 (2021).
[29] Y. H. Kwan, Y. Hu, S. H. Simon, and S. Parameswaran, *Excitonic Fractional Quantum Hall Hierarchy in Moiré Heterostructures*, arXiv:2003.11559.
[30] N. Stefanidis and I. Sodemann, *Excitonic Laughlin States in Ideal Topological Insulator Flat Bands and Their Possible Presence in Moiré Superlattice Materials*, Phys. Rev. B **102**, 035158 (2020).
[31] A. Belavin and A. Polyakov, *Metastable States of Two-Dimensional Isotropic Ferromagnets*, JETP Lett. **22**, 245 (1975), http://jetpletters.ru/ps/1529/article_23383.shtml.
[32] S. L. Sondhi, A. Karlhede, S. A. Kivelson, and E. H. Rezayi, *Skyrmions and the Crossover from the Integer to Fractional Quantum Hall Effect at Small Zeeman Energies*, Phys. Rev. B **47**, 16419 (1993).
[33] K. Moon, H. Mori, K. Yang, S. M. Girvin, A. H. MacDonald, L. Zheng, D. Yoshioka, and S.-C. Zhang, *Spontaneous Interlayer Coherence in Double-Layer Quantum Hall Systems: Charged Vortices and Kosterlitz-Thouless Phase Transitions*, Phys. Rev. B **51**, 5138 (1995).
[34] H. A. Fertig, L. Brey, R. Côté, and A. H. MacDonald, *Charged Spin-Texture Excitations and the Hartree-Fock Approximation in the Quantum Hall Effect*, Phys. Rev. B **50**, 11018 (1994).
[35] M. Abolfath, J. J. Palacios, H. A. Fertig, S. M. Girvin, and A. H. MacDonald, *Critical Comparison of Classical Field Theory and Microscopic Wave Functions for Skyrmions in Quantum Hall Ferromagnets*, Phys. Rev. B **56**, 6795 (1997).
[36] S. Chatterjee, N. Bultinck, and M. P. Zaletel, *Symmetry Breaking and Skyrmionic Transport in Twisted Bilayer Graphene*, Phys. Rev. B **101**, 165141 (2020).
[37] Y.-H. Zhang, D. Mao, Y. Cao, P. Jarillo-Herrero, and T. Senthil, *Nearly Flat Chern Bands in Moiré Superlattices*, Phys. Rev. B **99**, 075127 (2019).
[38] F. Wu and S. Das Sarma, *Quantum Geometry and Stability of Moiré Flatband Ferromagnetism*, Phys. Rev. B **102**, 165118 (2020).
[39] A. G. Abanov and P. B. Wiegmann, *Chiral Nonlinear σ Models as Models for Topological Superconductivity*, Phys. Rev. Lett. **86**, 1319 (2001).
[40] T. Grover and T. Senthil, *Topological Spin Hall States, Charged Skyrmions, and Superconductivity in Two Dimensions*, Phys. Rev. Lett. **100**, 156804 (2008).
[41] Y. Cao, D. Rodan-Legrain, J. M. Park, N. F. Q. Yuan, K. Watanabe, T. Taniguchi, R. M. Fernandes, L. Fu, and P. Jarillo-Herrero, *Nematicity and Competing Orders in Superconducting Magic-Angle Graphene*, Science **372**, 264 (2021).
[42] Y. Saito, J. Ge, K. Watanabe, T. Taniguchi, and A. F. Young, *Independent Superconductors and Correlated Insulators in Twisted Bilayer Graphene*, Nat. Phys. **16**, 926 (2020).
[43] P. Stepanov, I. Das, X. Lu, A. Fahimniya, K. Watanabe, T. Taniguchi, F. H. L. Koppens, J. Lischner, L. Levitov, and D. K. Efetov, *Untying the Insulating and Superconducting Orders in Magic-Angle Graphene*, Nature (London) **583**, 375 (2020).
[44] X. Liu, Z. Wang, K. Watanabe, T. Taniguchi, O. Vafek, and J. Li, *Tuning Electron Correlation in Magic-Angle Twisted*

Bilayer Graphene Using Coulomb Screening, Science **371**, 1261 (2021).

[45] M. Oh, K. P. Nuckolls, D. Wong, R. L. Lee, X. Liu, K. Watanabe, T. Taniguchi, and A. Yazdani, *Evidence for Unconventional Superconductivity in Twisted Bilayer Graphene*, Nature (London) **600**, 240 (2021).

[46] Y. H. Kwan, G. Wagner, N. Chakraborty, S. H. Simon, and S. A. Parameswaran, *Domain Wall Competition in the Chern Insulating Regime of Twisted Bilayer Graphene*, Phys. Rev. B **104**, 115404 (2021).

[47] R. Bistritzer and A. H. MacDonald, *Moiré Bands in Twisted Double-Layer Graphene*, Proc. Natl. Acad. Sci. U.S.A. **108**, 12233 (2011).

[48] J. M. B. Lopes dos Santos, N. M. R. Peres, and A. H. Castro Neto, *Graphene Bilayer with a Twist: Electronic Structure*, Phys. Rev. Lett. **99**, 256802 (2007).

[49] L. Brey, H. A. Fertig, R. Côté, and A. H. MacDonald, *Skyrme Crystal in a Two-Dimensional Electron Gas*, Phys. Rev. Lett. **75**, 2562 (1995).

[50] A. G. Green, I. I. Kogan, and A. M. Tsvelik, *Skyrmions in the Quantum Hall Effect at Finite Zeeman Coupling*, Phys. Rev. B **54**, 16838 (1996).

[51] T. Bömerich, L. Heinen, and A. Rosch, *Skyrmion and Tetarton Lattices in Twisted Bilayer Graphene*, Phys. Rev. B **102**, 100408(R) (2020).

[52] D. R. Nelson and J. M. Kosterlitz, *Universal Jump in the Superfluid Density of Two-Dimensional Superfluids*, Phys. Rev. Lett. **39**, 1201 (1977).

[53] P. J. Ledwith, E. Khalaf, and A. Vishwanath, *Strong Coupling Theory of Magic-Angle Graphene: A Pedagogical Introduction*, Ann. Phys. (Amsterdam) **435**, 168646 (2021).

[54] See Supplemental Material at http://link.aps.org/supplemental/10.1103/PhysRevX.12.031020 for details of the interacting BM model and the effective skyrmion hopping model.

[55] P. J. Ledwith, E. Khalaf, Z. Zhu, S. Carr, E. Kaxiras, and A. Vishwanath, *TB or not TB? Contrasting Properties of Twisted Bilayer Graphene and the Alternating Twist n-Layer Structures* ($n = 3, 4, 5, \ldots$), arXiv:2111.11060.

[56] N. N. T. Nam and M. Koshino, *Lattice Relaxation and Energy Band Modulation in Twisted Bilayer Graphene*, Phys. Rev. B **96**, 075311 (2017).

[57] S. Carr, S. Fang, Z. Zhu, and E. Kaxiras, *Exact Continuum Model for Low-Energy Electronic States of Twisted Bilayer Graphene*, Phys. Rev. Research **1**, 013001 (2019).

[58] G. Tarnopolsky, A. J. Kruchkov, and A. Vishwanath, *Origin of Magic Angles in Twisted Bilayer Graphene*, Phys. Rev. Lett. **122**, 106405 (2019).

[59] Z. Bi, N. F. Q. Yuan, and L. Fu, *Designing Flat Bands by Strain*, Phys. Rev. B **100**, 035448 (2019).

[60] D. E. Parker, T. Soejima, J. Hauschild, M. P. Zaletel, and N. Bultinck, *Strain-Induced Quantum Phase Transitions in Magic-Angle Graphene*, Phys. Rev. Lett. **127**, 027601 (2021).

[61] J. Jung, A. M. DaSilva, A. H. MacDonald, and S. Adam, *Origin of Band Gaps in Graphene on Hexagonal Boron Nitride*, Nat. Commun. **6**, 1 (2015).

[62] L. Zou, H. C. Po, A. Vishwanath, and T. Senthil, *Band Structure of Twisted Bilayer Graphene: Emergent Symmetries, Commensurate Approximants, and Wannier Obstructions*, Phys. Rev. B **98**, 085435 (2018).

[63] Z. Song, Z. Wang, W. Shi, G. Li, C. Fang, and B. A. Bernevig, *All Magic Angles in Twisted Bilayer Graphene Are Topological*, Phys. Rev. Lett. **123**, 036401 (2019).

[64] K. Hejazi, X. Chen, and L. Balents, *Hybrid Wannier Chern Bands in Magic Angle Twisted Bilayer Graphene and the Quantized Anomalous Hall Effect*, Phys. Rev. Research **3**, 013242 (2021).

[65] M. Xie and A. H. MacDonald, *Nature of the Correlated Insulator States in Twisted Bilayer Graphene*, Phys. Rev. Lett. **124**, 097601 (2020).

[66] S. Liu, E. Khalaf, J. Y. Lee, and A. Vishwanath, *Nematic Topological Semimetal and Insulator in Magic-Angle Bilayer Graphene at Charge Neutrality*, Phys. Rev. Research **3**, 013033 (2021).

[67] P. J. Ledwith, G. Tarnopolsky, E. Khalaf, and A. Vishwanath, *Fractional Chern Insulator States in Twisted Bilayer Graphene: An Analytical Approach*, Phys. Rev. Research **2**, 023237 (2020).

[68] A. Kerelsky, L. J. McGilly, D. M. Kennes, L. Xian, M. Yankowitz, S. Chen, K. Watanabe, T. Taniguchi, J. Hone, C. Dean *et al.*, *Maximized Electron Interactions at the Magic Angle in Twisted Bilayer Graphene*, Nature (London) **572**, 95 (2019).

[69] Y. Choi, J. Kemmer, Y. Peng, A. Thomson, H. Arora, R. Polski, Y. Zhang, H. Ren, J. Alicea, G. Refael *et al.*, *Electronic Correlations in Twisted Bilayer Graphene near the Magic Angle*, Nat. Phys. **15**, 1174 (2019).

[70] Y. Jiang, X. Lai, K. Watanabe, T. Taniguchi, K. Haule, J. Mao, and E. Y. Andrei, *Charge Order and Broken Rotational Symmetry in Magic-Angle Twisted Bilayer Graphene*, Nature (London) **573**, 91 (2019).

[71] Y. Xie, B. Lian, B. Jäck, X. Liu, C.-L. Chiu, K. Watanabe, T. Taniguchi, B. A. Bernevig, and A. Yazdani, *Spectroscopic Signatures of Many-Body Correlations in Magic Angle Twisted Bilayer Graphene*, Nature (London) **572**, 101 (2019).

[72] D. Wong, K. P. Nuckolls, M. Oh, B. Lian, Y. Xie, S. Jeon, K. Watanabe, T. Taniguchi, B. A. Bernevig, and A. Yazdani, *Cascade of Electronic Transitions in Magic-Angle Twisted Bilayer Graphene*, Nature (London) **582**, 198 (2020).

[73] K. Lejnell, A. Karlhede, and S. L. Sondhi, *Effective-Action Studies of Quantum Hall Spin Textures*, Phys. Rev. B **59**, 10183 (1999).

[74] K. N. Kudin, G. E. Scuseria, and E. Cancès, *A Black-Box Self-Consistent Field Convergence Algorithm: One Step Closer*, J. Chem. Phys. **116**, 8255 (2002).

[75] M. Xie and A. H. MacDonald, *Weak-Field Hall Resistivity and Spin-Valley Flavor Symmetry Breaking in Magic-Angle Twisted Bilayer Graphene*, Phys. Rev. Lett. **127**, 196401 (2021).

[76] T. Cea and F. Guinea, *Band Structure and Insulating States Driven by Coulomb Interaction in Twisted Bilayer Graphene*, Phys. Rev. B **102**, 045107 (2020).

[77] Y. Zhang, K. Jiang, Z. Wang, and F. Zhang, *Correlated Insulating Phases of Twisted Bilayer Graphene at Commensurate Filling Fractions: A Hartree-Fock Study*, Phys. Rev. B **102**, 035136 (2020).

[78] J. Kang and O. Vafek, *Non-Abelian Dirac Node Braiding and Near-Degeneracy of Correlated Phases at Odd Integer Filling in Magic-Angle Twisted Bilayer Graphene*, Phys. Rev. B **102**, 035161 (2020).
[79] F. Xie, A. Cowsik, Z.-D. Song, B. Lian, B. A. Bernevig, and N. Regnault, *Twisted Bilayer Graphene. VI. An Exact Diagonalization Study at Nonzero Integer Filling*, Phys. Rev. B **103**, 205416 (2021).
[80] T. Soejima, D. E. Parker, N. Bultinck, J. Hauschild, and M. P. Zaletel, *Efficient Simulation of Moiré Materials Using the Density Matrix Renormalization Group*, Phys. Rev. B **102**, 205111 (2020).
[81] P. Potasz, M. Xie, and A. H. MacDonald, *Exact Diagonalization for Magic-Angle Twisted Bilayer Graphene*, Phys. Rev. Lett. **127**, 147203 (2021).
[82] J. Liu and X. Dai, *Theories for the Correlated Insulating States and Quantum Anomalous Hall Effect Phenomena in Twisted Bilayer Graphene*, Phys. Rev. B **103**, 035427 (2021).
[83] G. Shavit, E. Berg, A. Stern, and Y. Oreg, *Theory of Correlated Insulators and Superconductivity in Twisted Bilayer Graphene*, Phys. Rev. Lett. **127**, 247703 (2021).
[84] S. Zhang, X. Lu, and J. Liu, *Correlated Insulators, Density Wave States, and Their Nonlinear Optical Response in Magic-Angle Twisted Bilayer Graphene*, Phys. Rev. Lett. **128**, 247402 (2022).
[85] K. Hejazi, C. Liu, H. Shapourian, X. Chen, and L. Balents, *Multiple Topological Transitions in Twisted Bilayer Graphene near the First Magic Angle*, Phys. Rev. B **99**, 035111 (2019).
[86] J. Kang, B. A. Bernevig, and O. Vafek, *Cascades between Light and Heavy Fermions in the Normal State of Magic Angle Twisted Bilayer Graphene*, Phys. Rev. Lett. **127**, 266402 (2021).
[87] A. T. Pierce, Y. Xie, J. M. Park, E. Khalaf, S. H. Lee, Y. Cao, D. E. Parker, P. R. Forrester, S. Chen, K. Watanabe, T. Taniguchi, A. Vishwanath, P. Jarillo-Herrero, and A. Yacoby, *Unconventional Sequence of Correlated Chern Insulators in Magic-Angle Twisted Bilayer Graphene*, Nat. Phys. **17**, 1210 (2021).
[88] F. Guinea and N. R. Walet, *Electrostatic Effects, Band Distortions, and Superconductivity in Twisted Graphene Bilayers*, Proc. Natl. Acad. Sci. U.S.A. **115**, 13174 (2018).
[89] L. Rademaker, D. A. Abanin, and P. Mellado, *Charge Smoothening and Band Flattening Due to Hartree Corrections in Twisted Bilayer Graphene*, Phys. Rev. B **100**, 205114 (2019).
[90] T. Cea, N. R. Walet, and F. Guinea, *Electronic Band Structure and Pinning of Fermi Energy to van Hove Singularities in Twisted Bilayer Graphene: A Self-Consistent Approach*, Phys. Rev. B **100**, 205113 (2019).
[91] Z. A. H. Goodwin, V. Vitale, X. Liang, A. A. Mostofi, and J. Lischner, *Hartree Theory Calculations of Quasiparticle Properties in Twisted Bilayer Graphene*, arXiv:2004.14784.
[92] Y. Lian and M. O. Goerbig, *Spin-Valley Skyrmions in Graphene at Filling Factor $\nu = -1$*, Phys. Rev. B **95**, 245428 (2017).
[93] J. Atteia, Y. Lian, and M. O. Goerbig, *Skyrmion Zoo in Graphene at Charge Neutrality in a Strong Magnetic Field*, Phys. Rev. B **103**, 035403 (2021).
[94] A. J. Nederveen and Y. V. Nazarov, *Skyrmions in Disordered Heterostructures*, Phys. Rev. Lett. **82**, 406 (1999).
[95] J. Sinova, A. H. MacDonald, and S. M. Girvin, *Disorder and Interactions in Quantum Hall Ferromagnets near $\nu = 1$*, Phys. Rev. B **62**, 13579 (2000).
[96] S. Rapsch, J. T. Chalker, and D. K. K. Lee, *Spin Textures, Screening, and Excitations in Dirty Quantum Hall Ferromagnets*, Phys. Rev. Lett. **88**, 036801 (2002).
[97] D. K. K. Lee, S. Rapsch, and J. T. Chalker, *Dirty Quantum Hall Ferromagnets and Quantum Hall Spin Glasses*, Phys. Rev. B **67**, 195322 (2003).
[98] H. A. Fertig and G. Murthy, *Coherence Network in the Quantum Hall Bilayer*, Phys. Rev. Lett. **95**, 156802 (2005).
[99] J. H. Wilson, Y. Fu, S. Das Sarma, and J. H. Pixley, *Disorder in Twisted Bilayer Graphene*, Phys. Rev. Research **2**, 023325 (2020).
[100] A. Uri, S. Grover, Y. Cao, J. A. Crosse, K. Bagani, D. Rodan-Legrain, Y. Myasoedov, K. Watanabe, T. Taniguchi, P. Moon *et al.*, *Mapping the Twist-Angle Disorder and Landau Levels in Magic-Angle Graphene*, Nature (London) **581**, 47 (2020).
[101] S. E. Barrett, G. Dabbagh, L. N. Pfeiffer, K. W. West, and R. Tycko, *Optically Pumped NMR Evidence for Finite-Size Skyrmions in GaAs Quantum Wells near Landau Level Filling $\nu = 1$*, Phys. Rev. Lett. **74**, 5112 (1995).
[102] D. Călugăru, N. Regnault, M. Oh, K. P. Nuckolls, D. Wong, R. L. Lee, A. Yazdani, O. Vafek, and B. A. Bernevig, *Spectroscopy of Twisted Bilayer Graphene Correlated Onsulators*, arXiv:2110.15300.
[103] J. P. Hong, T. Soejima, and M. P. Zaletel, *Detecting Symmetry Breaking in Magic Angle Graphene Using Scanning Tunneling Microscopy*, arXiv:2110.14674.
[104] S.-Y. Li, Y. Zhang, L.-J. Yin, and L. He, *Scanning Tunneling Microscope Study of Quantum Hall Isospin Ferromagnetic States in the Zero Landau Level in a Graphene Monolayer*, Phys. Rev. B **100**, 085437 (2019).
[105] X. Liu, G. Farahi, C.-L. Chiu, Z. Papic, K. Watanabe, T. Taniguchi, M. P. Zaletel, and A. Yazdani, *Visualizing Broken Symmetry and Topological Defects in a Quantum Hall Ferromagnet*, Science **375**, 321 (2022).
[106] A. Coissard, D. Wander, H. Vignaud, A. G. Grushin, C. Repellin, K. Watanabe, T. Taniguchi, F. Gay, C. Winkelmann, H. Courtois, H. Sellier, and B. Sacépé, *Imaging Tunable Quantum Hall Broken-Symmetry Orders in Charge-Neutral Graphene*, Nature (London) **605**, 51 (2022).
[107] Y. Cao, D. Rodan-Legrain, O. Rubies-Bigorda, J. M. Park, K. Watanabe, T. Taniguchi, and P. Jarillo-Herrero, *Tunable Correlated States and Spin-Polarized Phases in Twisted Bilayer–Bilayer Graphene*, Nature (London) **583**, 215 (2020).
[108] C. Shen, Y. Chu, Q. Wu, N. Li, S. Wang, Y. Zhao, J. Tang, J. Liu, J. Tian, K. Watanabe *et al.*, *Correlated States in Twisted Double Bilayer Graphene*, Nat. Phys. **16**, 520 (2020).
[109] X. Liu, Z. Hao, E. Khalaf, J. Y. Lee, Y. Ronen, H. Yoo, D. H. Najafabadi, K. Watanabe, T. Taniguchi, A. Vishwanath *et al.*, *Tunable Spin-Polarized Correlated States in Twisted Double Bilayer Graphene*, Nature (London) **583**, 221 (2020).

[110] G. Chen, A. L. Sharpe, P. Gallagher, I. T. Rosen, E. J. Fox, L. Jiang, B. Lyu, H. Li, K. Watanabe, T. Taniguchi *et al.*, *Signatures of Tunable Superconductivity in a Trilayer Graphene Moiré Superlattice*, Nature (London) **572**, 215 (2019).

[111] E. Khalaf, A. J. Kruchkov, G. Tarnopolsky, and A. Vishwanath, *Magic Angle Hierarchy in Twisted Graphene Multilayers*, Phys. Rev. B **100**, 085109 (2019).

[112] J. M. Park, Y. Cao, K. Watanabe, T. Taniguchi, and P. Jarillo-Herrero, *Tunable Strongly Coupled Superconductivity in Magic-Angle Twisted Trilayer Graphene*, Nature (London) **590**, 249 (2021).

[113] H. Kim, Y. Choi, C. Lewandowski, A. Thomson, Y. Zhang, R. Polski, K. Watanabe, T. Taniguchi, J. Alicea, and S. Nadj-Perge, *Spectroscopic Signatures of Strong Correlations and Unconventional Superconductivity in Twisted Trilayer Graphene*, arXiv:2109.12127.

[114] E. Khalaf and A. Vishwanath, *From Electrons to Baby Skyrmions in Chern Ferromagnets: A Topological Mechanism for Spin-Polaron Formation in Twisted Bilayer Graphene*, arXiv:2112.06935.

[115] F. Schindler, O. Vafek, and B. A. Bernevig, *Trions in Twisted Bilayer Graphene*, Phys. Rev. B **105**, 155135 (2022).